

AD-A168 450

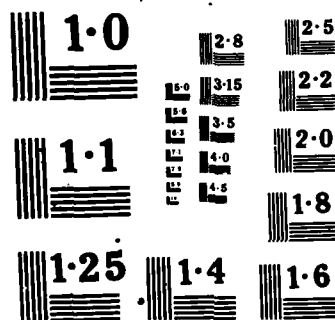
ACTA AERONAUTICA ET ASTRONAUTICA SINICA (SELECTED
ARTICLES)(U) FOREIGN TECHNOLOGY DIV WRIGHT-PATTERSON
AFB OH M LIU ET AL 29 MAY 86 FTD-ID(RS)T-1275-85

F/G 20/4

1/2

UNCLASSIFIED

ML



NATIONAL BUREAU OF STANDARDS
MICROCOPY RESOLUTION TEST

2

FTD-ID(RS)T-1265-85

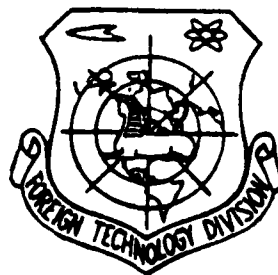
AD-A168 450

FOREIGN TECHNOLOGY DIVISION



DTIC
SELECTED
JUN 17 1986
S D

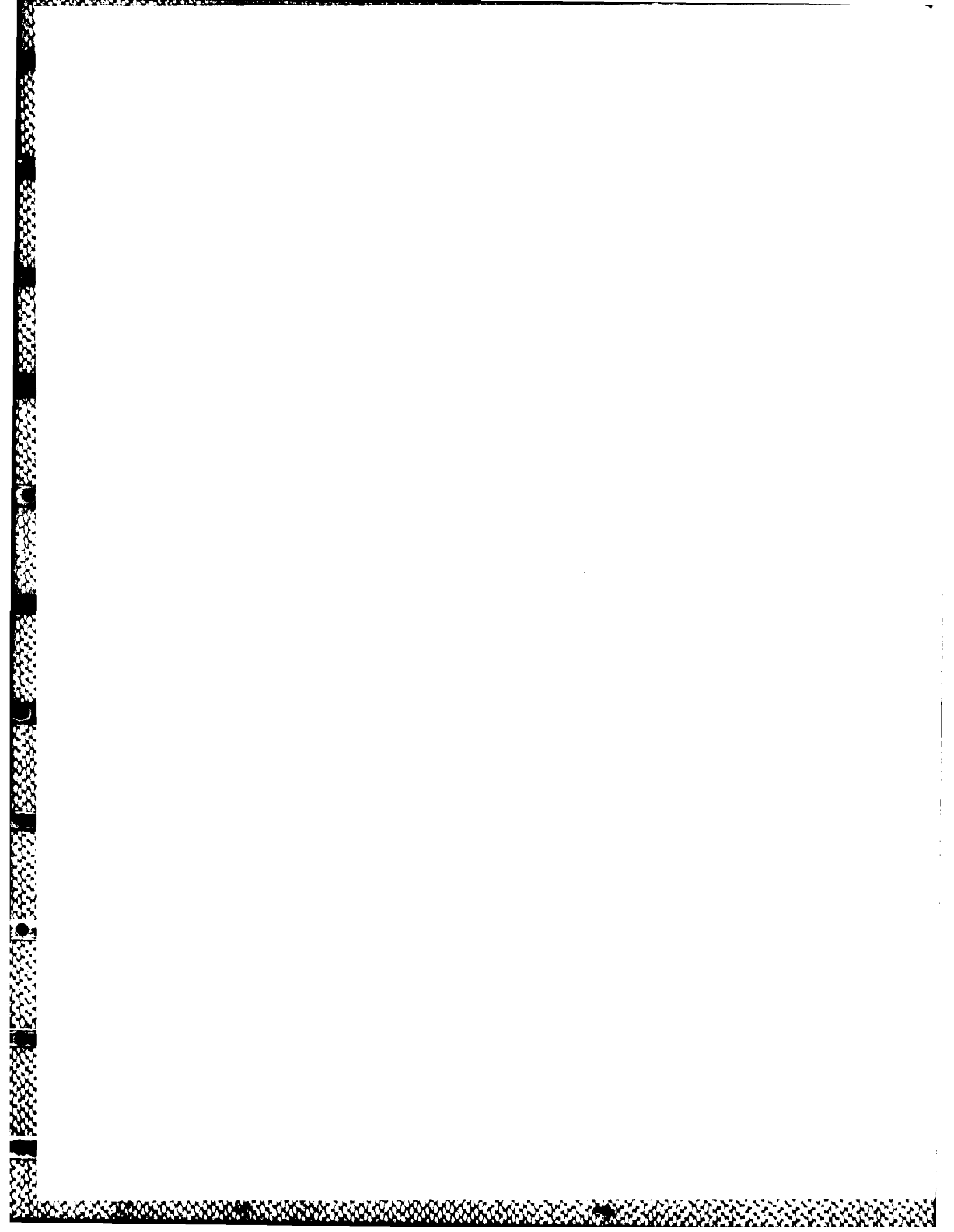
ACTA AERONAUTICA ET ASTRONAUTICA SINICA
(Selected Articles)



DTIC FILE COPY

Approved for public release;
Distribution unlimited.

86 6 16 06



HUMAN TRANSLATION

FTD-ID(RS)T-1265-85

29 May 1986

MICROFICHE NR: FTD-86-C-001881

ACTA AERONAUTICA ET ASTRONAUTICA SINICA
(Selected Articles)

English pages: 94

Source: Hang Kong Xuebao, Vol. 6, Nr. 1, February
1985, pp. 1-20; 29-37; 49-74

Country of origin: China

Translated by: SCITRAN

F33657-84-D-0165

Approved for public release; distribution unlimited.

THIS TRANSLATION IS A RENDITION OF THE ORIGINAL FOREIGN TEXT WITHOUT ANY ANALYTICAL OR EDITORIAL COMMENT. STATEMENTS OR THEORIES ADVOCATED OR IMPLIED ARE THOSE OF THE SOURCE AND DO NOT NECESSARILY REFLECT THE POSITION OR OPINION OF THE FOREIGN TECHNOLOGY DIVISION.

PREPARED BY:

TRANSLATION DIVISION
FOREIGN TECHNOLOGY DIVISION
WPAFB, OHIO

Table of Contents

Graphics Disclaimer	ii
Development in Vortex Motion Research, by Liu Mouji, Su Wenhan	1
Application of New Type of Pole Collocation Equations to Determining Laws Controlling a Bi-input Multi-output System, by Lu Shuquen	32
Quick Geometry Generation and Surface Mesh Partition for Arbitrary 3-D Bodies, by Tang, Zinqing, Li Anqui, Cao Shujiang	47
Numerical Calculation of Flow Field in Afterburner Diffuser of Turbofan Engine, by Chen Yiliang	63
Design of an Airborne Optic Fiber Data Bus System, by Fan Renzhou, Wang Gonghao, Chen Ruilin	75

Accession For	
NTIS CRA&I	<input checked="" type="checkbox"/>
DTIC TAB	<input type="checkbox"/>
Unannounced	<input type="checkbox"/>
Justification	
By	
Distribution/	
Availability Codes	
Dist	Avail and/or Special
A-1	



GRAPHICS DISCLAIMER

All figures, graphics, tables, equations, etc. merged into this translation were extracted from the best quality copy available.

Development in Vortex Motion Research

/1

Liu Mouji and Su Wenhan

(Beijing Institute of Aeronautics and Astronautics)

Abstract

This paper briefly introduces the results of vortex motion research in the following areas: nine types of separated flows and boundaries of delta wings with various sweepbacks and angles of attack at low speeds, analysis of three-dimensional separated flow and vortex flow based on qualitative theory of differential equations and topology, vortex breakdown patterns, experimental study and theoretical analysis on the leading edge vortex breakdown of delta wings, controlled separation and vortex interference, and the displacement, rotation and recombination of two vortices.

Introduction

The study of vortex motion is a classic subject in fluid dynamics. Its theory has already become an integral part in fluid dynamics. In recent years, due to the need in developing civil and military aircrafts, the concept of aerodynamic design has extended from avoiding flow separation to utilizing controlled separation. The emergence of slender wing, double

delta wing, strake wing, nearly coupled duck wing and leading edge vortex flap, the study of spanwise flow, the generation and elimination of lateral force on slender body at large attack angles, the study of various complex flows at large attack angles, the danger of large aspect ratio wing trailing vortex on the aircraft behind it, the study of rotational flow characteristics of helicopters, the investigation of turbulent structure and its transformation mechanism, and the studies on vortex flows for non-aviation applications impose new requirements on the research of vortex motion. There are many papers concerning the experimental study, numerical calculation and theoretical analysis aspects of the problem. In addition, there are numerous review and symposium papers^[1-8]. In this paper, results regarding the following problems are briefly introduced. They are the type and boundary of leading edge separated flows of delta wings, topological analysis on vortex and separated flow, problems regarding the breakdown of vortices, and controlled separation and interference of vortex.

I. Type and Boundary of Leading Edge Separated Flow of Delta Wing

A profound understanding of the flow pattern is the basis of the study and design of aerodynamics. A great deal of work has been done already^[9-16]. Due to the maneuverability requirement at large attack angles, it is necessary to understand the flow pattern around the aircraft within the range of attack angles

from $0 \sim 90^\circ$. For this reason, it is meaningful to study various possible flow patterns and to understand their distinction, correlation and transition.

We conducted low velocity oil flow and smoke line experiments for a series of sharp leading edge flat delta wings with sweepback from $15 \sim 85^\circ$ in the range of attack angle of $0 \sim 90^\circ$. Based on these results, we obtained nine types of separated flows and their boundaries on the leeward wing surface.

The typical flow pattern on the lower surface of a sharp leading edge delta wing is shown in Figure 1. At small attack angles, the left and right adhesion lines are both near the leading edge. At large angles of attack, however, these two lines coincide in the middle at the front portion of the wing. The larger the angle of attack is, the more the termination point of the coincided line moves downstream. However, they always remain as two lines.

Manuscript received on June 19, 1984.

The flow pattern on the upper wing surface varies with the leading edge sweepback and angle of attack in a more complicated manner. In addition to boundary flow, there are nine different separated flows in total.

1. Leading Edge Bubble: The shear layer dragged away due to leading edge separation is adhered to the upper wing surface to form a bubble. The bubble is a viscid region which is approximately parallel to the leading edge. There is a spiral flow to some extent in the bubble, as shown in Figure 2.

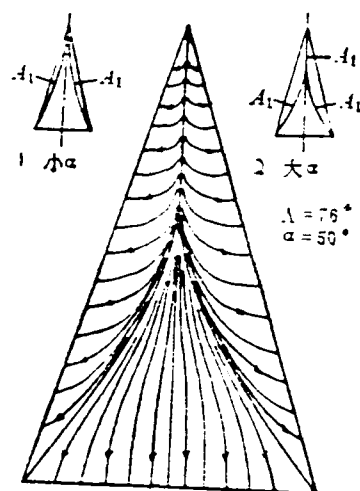


Figure 1. Flow Pattern on Lower Surface of Delta Wing
($\Lambda = 76^\circ$, $\alpha = 55^\circ$)

1. small α
2. large α

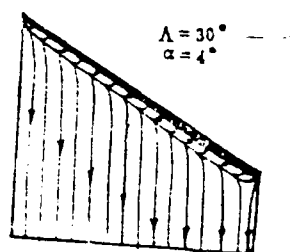


Figure 2. The Bubble

2. Bubble Vortex: With increasing angle of attack, the bubble on a medium sweepback delta wing is converted into a bubble vortex. In this case, the shear layer from leading edge separation will not re-adhere to the upper wing surface. Instead, it begins to roll up to form a spiral vortex surface. Based on observation of the spatial flow pattern, the bubble vortex does not have a nucleus. Its surface flow pattern is shown in Figure 3.

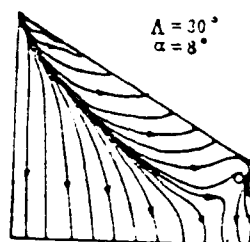


Figure 3. Bubble Vortex

3. Streamwise Vortex: As the angle of attack increases, streamwise vortices begin to appear on large sweepback delta wings in two arrays as shows in Figure 4. They more or less follow the direction of the flow; from the leading edge to the trailing edge. The direction of rotation on the right is counterclockwise and it is the opposite on the left.

4. Concentrated Vortex: As the angle of attack increases, concentrated vortex begins to slow up on a delta wing with a large sweepback, as shown in Figure 5. In this case, the free shear layer from the leading edge separation line has already rolled up to form a spiral vortex. One end of the vortex is always connected to the object (at the line of separation). The other end, however, is rolled up into a highly concentrated vortex nucleus (which is in a free state). This nucleus passes beyond the trailing edge to far away downstream. This phenomenon could be clearly seen in spatial flow pattern observations. In this case, the vortex from the separation line at the surface of the object is sufficient to move along with the nucleus. Hence, the flow is stable. A concentrated vortex is a steady vortex flow.

5. Bursting Vortex: At a certain angle of attack, the vortex bursting point of a concentrated vortex appears downstream far away from the trailing edge. Afterward, it moves forward as the angle of attack increases and passes over the trailing edge to the wing surface. It moves further to the apex of the wing. The burst vortex between the trailing edge and the wing apex is called bursting vortex. In front of the bursting point, the nucleus of the vortex still exists. Figure 6 shows the flow pattern of a bursting vortex on a medium sweepback wing. In this case, a vortex is present in front of the spiral point. Beyond the spiral point, we see a return flow. When the concentrated vortex of a large sweepback delta wing begins to burst, the

secondary separation line of the surface of the object will bend outward.

6. Spiral Flow: When the bursting point reaches the apex of the wing, the nucleus disappears completely. As the angle of attack increases, a spiral flow will emerge. The upper wing flow pattern does not have a vortex. There is only a return flow with an apparent spiral point, as shown in Figure 7. Based on observing spatial flow pattern we know that the separated flow on the leeward surface is rising spirally upward in a unsteady manner near the spiral point. The vortex moment is escaping in an unsteady manner from the spiral point. The spiral flow is an unsteady flow. /3

7. Reversed Flow: When the angle of attack increases further, reversed flow will occur. In this case, the flow near the wing surface is basically moving from the rear to the front. The flow pattern on the surface is shown in Figure 8. The re-adhesion point of the leading edge separated vortex is very close to the trailing edge. The reversed flow is splitting into two near the leading edge at the middle of the wing; one going inward and the other outward. Reversed flow is an unsteady flow.

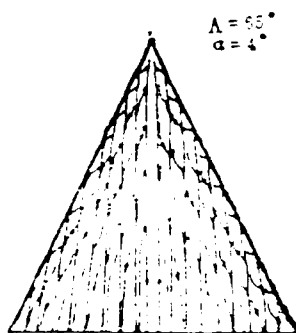


Figure 4. Streamwise Vortex

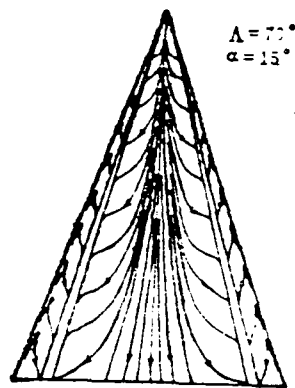


Figure 5. Concentrated Vortex

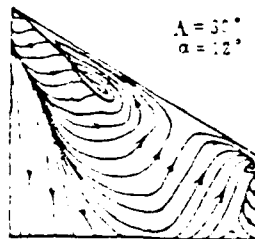


Figure 6. Bursting Vortex

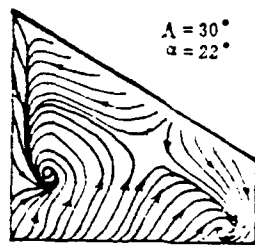


Figure 7. Spiral Flow

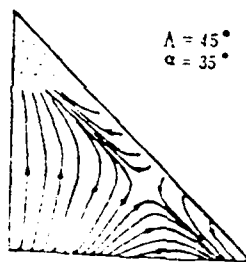


Figure 8. Reversed Flow

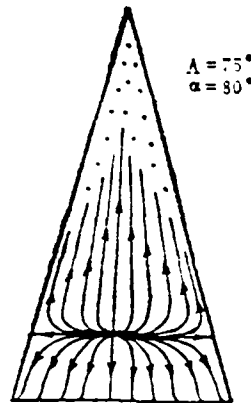


Figure 9. Completely Separated Flow

8. Completely Separated Flow: When the angle of attack is very large, the re-adhesion point near the trailing edge moves forward to the wing surface to create complete separation, as shown in Figure 9. This indicates that the trailing edge vortex has already appeared near the wing surface. This vortex may be observed by symmetric oil flowing plate or smoke line method. Completely separated flow is also unsteady.

9. Asymmetric Vortex: If the leading edge sweepback of the wing is very large, such as more than 80° , the two opposite vortices will create an asymmetric flow pattern (See Figure 10). Based on the figure we can see that the re-adhesion line is no longer at the center of the wing. Instead, it first intersects with one edge and then with the other. It appears as a saw tooth. On a large sweepback delta wing, concentrated vortex and bursting vortex may be asymmetric.

Based on the classification of flows described above, it is possible to determine the flow boundaries of various types of separated flows on the (Λ, α) plane, as shown in Figure 11. The major special feature is that the bursting point of any medium sweepback delta wing is always in front of the trailing edge of the wing and concentrated vortex will not appear at any attack angles. Large sweepback delta wings, however will show stable concentrated vortex with a specific range of attack angles. Bursting vortex, spiral flow, reversed flow and completely separated flow may also occur. However, as compared to a delta wing with a medium sweepback, the occurrence is delayed to a larger angle of attack. A slender delta wing will have an asymmetric vortex, similar to the case of a slender revolving body. From Figure 11 we can see that at a certain attack angle (such as 15°), the spiral flow will change into a bursting vortex, or even a concentrated vortex, as the leading edge sweepback increases. This change from an unfavorable unsteady separated flow to a favorable steady vortex is the design of controlled separation of slender wing.

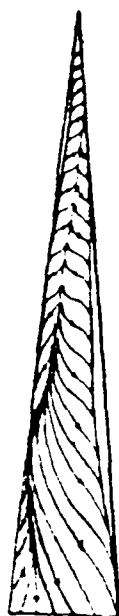


Figure 10. Asymmetric Vortex

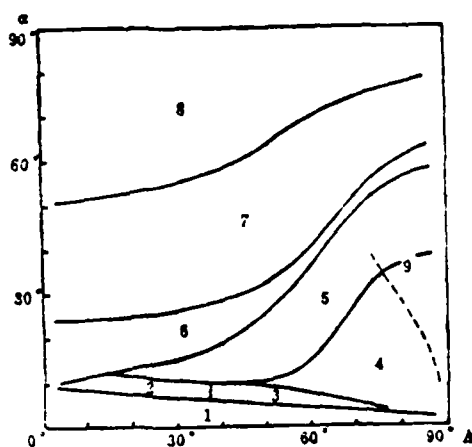


Figure 11. Types of Separated Flow Patterns and Their Boundaries of Leading Edge Separation of Delta Wing at Low Velocity

1. bubble
2. bubble vortex
3. streamwise vortex
4. concentrated vortex
5. bursting vortex
6. spiral vortex
7. reversed flow
8. completely separated flow
9. asymmetric vortex

It should be pointed out that dull leading edge delta wings have different separated flow and vortices^[14].

II. Topological Analysis on Vortex and Separated Flow

Qualitative theory of differential equations and topology is a useful tool to analyze flow patterns in studying three-dimensional separated flows and vortices. It has practical significance in studying the separation mechanism, establishing theoretical models and performing aerodynamic designs. Some people call it the topology for separated flow.

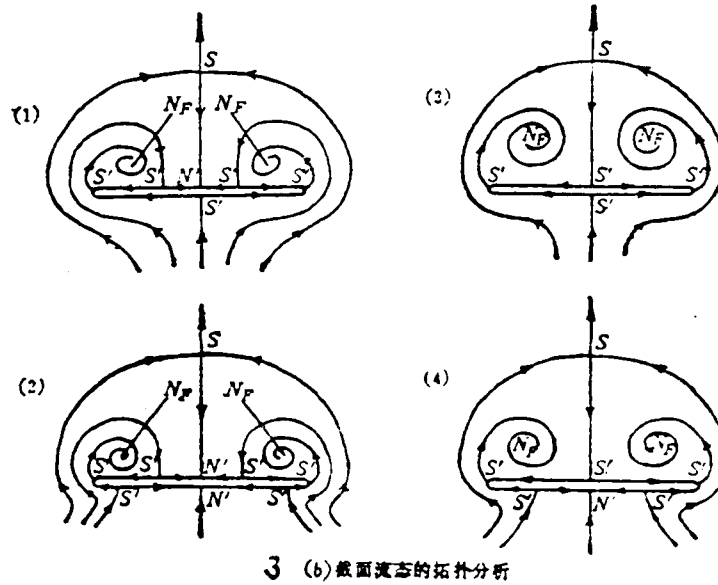
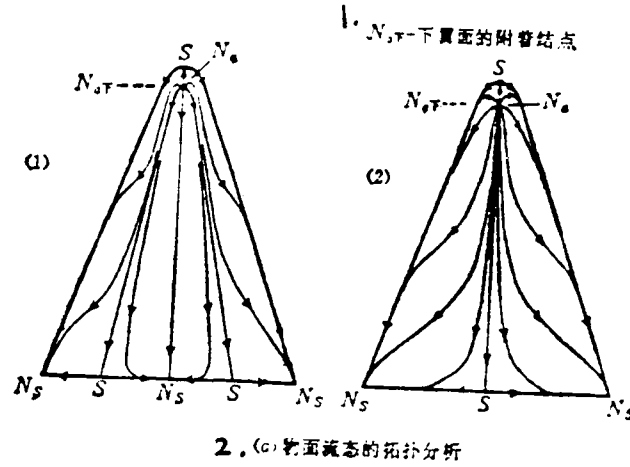


图12 三角翼集中涡流态的拓扑分析

4 (a) 上表面流态

5 典型流态	(i)	(ii)
$\Sigma v - \Sigma s$	5 - 3	4 - 2

6 (b) 截面流态

7 典型流态	(1)	(2)	(3)	(4)
$(\Sigma v + \frac{1}{2} \Sigma v') - (\Sigma s + \frac{1}{2} \Sigma s')$	2.5 - 3.5	3 - 4	2 - 3	2.5 -

Figure 12. Topological Analysis of Concentrated Vortex Flow Pattern on Delta Wing

1. $N_{a\text{low}}$ - nodal point of adhesion on lower wing surface
2. (a) topological analysis of surface flow pattern
3. (b) topological analysis of sectional flow pattern
4. (a) upper surface flow pattern
5. typical flow pattern
6. (b) sectional flow pattern
7. typical flow pattern

Up until now, studies on separated flow based on this method^[17-24] approximately include three aspects. One is to study the local pattern of separated flow near a singular point. There has been a great deal of work done in this area. The second area is to study the overall pattern (including the distribution of singular points over a wide range) of separated flow. In this regard, topological laws to be obeyed by the structure of separated flow under certain conditions were found. These laws have been used to analyze the topological structures of separated flows around some simple objects (such as delta wing, rectangular wing, semi-spherical cylinder, etc.). This type of analysis, however, must be performed based on raw flow spectrum obtained experimentally or from numerical calculation. The third area is to study the variation of the topological structure of a separated flow with parameters (such as α , Λ , R_e , M , etc.). This is a difficult subject. Some researchers are attempting to use abrupt change theory and structural stability theory of differential dynamic system to study these problems. To date, there is little accomplishment in this area.

We used the method described above to study the topological structures of various separated flows on delta wings with medium to large sweepbacks based on observations of flow patterns. Figure 12 shows the topological analysis of a concentrated vortex at the surface of the object and at its cross-section. For a simple body, the topological law for the singular points in the flow pattern on its surface is $\Sigma_N - \Sigma_S = 2$; where Σ_N is the total number of nodes and Σ_S is the total number of settle points. The topological law for singular points in the sectional flow pattern is $(\Sigma_N + 1/2\Sigma_{N'}) - (\Sigma_S + 1/2\Sigma_{S'}) = -1$, where $\Sigma_{N'}$ and $\Sigma_{S'}$ are the total number of semi-nodes and semi-settle points, respectively. N_{alow} is the node adhered to the lower wing surface. The analysis in the figure agrees with these two laws. Figure 13 shows the spiral flow on a 30° sweep delta wing. From the topological analysis we know that there are 13 nodes (including 5 attached nodes, 4 separated nodes and 4 separated spiral points) on the surface. In addition, there are 11 settle points. This agrees with the topological law governing the surface flow pattern.

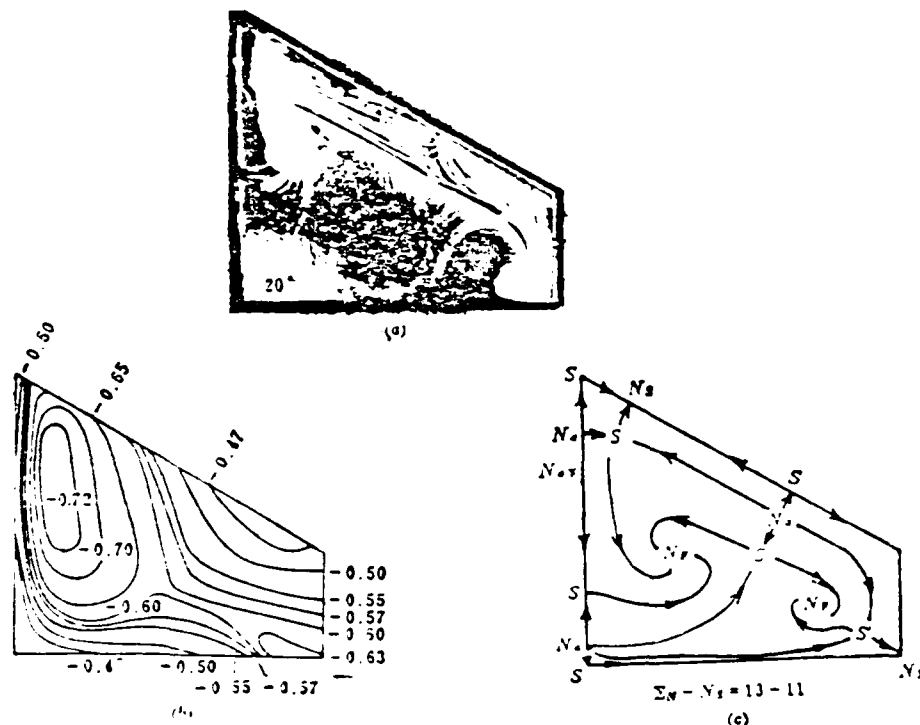


Figure 13. Spiral Flow on Sharply Cut Delta Wing with 30° Sweepback

- (a) upper surface flow pattern
- (b) upper surface isobars
- (c) topological analysis diagram

III. Problems Concerning Vortex Breakdown

17

The spatial pattern of vortex breakdown can primarily be classified as the spiral type and the bubble-like type. In addition, other types were also found in experiments. It was pointed out in reference [27] that the vortex breakdown patterns inside the tube include the spiral type, the bubble-like type and the double spiral type. In reference [30], six types of patterns were observed. It was pointed out in reference [25] that the leading edge vortex breakdown of a delta wing includes the spiral type and the bubble-like type. Based on the water tunnel experiment reported in reference [35], there are three types;

i.e., asymmetric spiral, symmetric bubble which bursts suddenly and gradually dissipating cone, as shown in Figure 14.

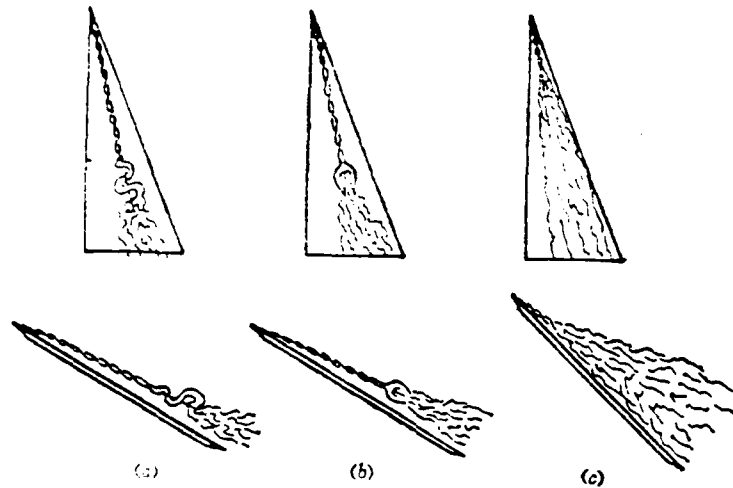


Figure 14. Three Types of Vortex Breakdown Patterns

- (a) spiral type
- (b) bubble-like type
- (c) conical type

In reference [30], the axial symmetric vortex breakdown flow field in the tube was measured by a laser velocity measuring technique. It includes the approaching flow area of the concentrated vortex, the breakdown area and the wake area. The breakdown area includes a decelerating area, a recirculation area and an axial flow restoration area. The time averaged flow pattern of the recirculation area is shown in Figure 15. It is a double cell structure with 4 stationary points. The flow in the recirculation area is unsteady. In reference [33], the spiral breakdown flow field of a vortex in the tube was obtained using a laser velocity determination method.

In reference [29], line of heat was used to measure the flow field in front and behind the breakdown of a leading edge vortex of a delta wing. The radial distribution of its axial velocity is shown in Figure 16. The distribution appears as a jet before the breakdown. Downstream from the breakdown point, it is in a wake-like shape. The fundamental change from a jet-like to a wake-like shape can be used as a criteria to determine the breakdown position. Vortex breakdown is related to axial velocity/circumferential velocity, inverse pressure gradient, flow tube expansion angle and Reynolds number. Its theoretical analysis is more or less based on the dynamic instability of the fluid, quasi-cylindrical approximation and finite transition theory[28]. These theories, which were originally proposed in the early 1960's, have been further developed. However, we still do not have a unified vortex breakdown theory to be recognized all over the world. In reference [31], the axisymmetric vortex breakdown in a uniform flow was studied by the numerical integration of the Navier-Stokes equation. In some references, the breakdown theory is combined with solving the flow field outside the leading edge vortex nucleus for analysis. For example, in reference [32], the theory of dynamic instability of the fluid was combined with the non-linear conical flow theory to analyze and calculate the leading edge vortex breakdown of delta wings. A comparison of these results to the experimental ones is shown in Figure 17. In the figure, K is a velocity type of parameter. Based on the result obtained from the dynamic

instability of the fluid, it is unsteady when $K < 1.16$. Based on the figure we see that the theory agrees with the experiment for delta wings with small aspect ratios. Vortex breakdown of delta wings was also investigated in reference [34].

The breakdown point of the leading edge vortex moves upstream as the angle of attack increases, until reaching the apex of the wing. The way the breakdown point moves upstream is related to the planar shape of the wings^[35] as shown in Figure 18. For slender wings, when the breakdown point moves across the trailing edge upstream, it travels very fast. Then it gradually slows down. For strake wings, however, the breakdown point also moves very fast when it passes the trailing edge of the wing and then it slows down. But it begins to move fast again after passing through the inflection point at the leading edge. Then it slows down again. It is a non-monotonic variation.

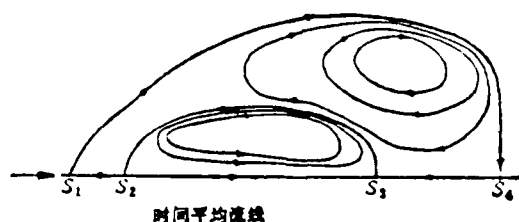


Figure 15. Double-Cell Structure in Recirculation Zone^[30]

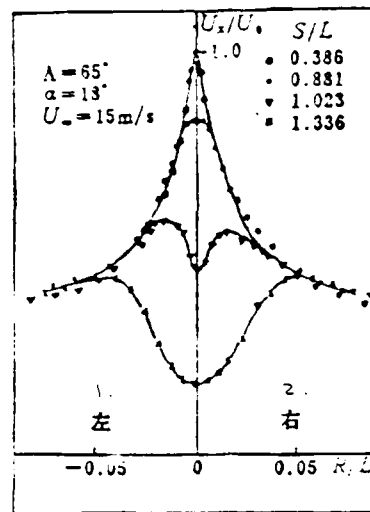


Figure 16. Distribution of Axial Velocity Before and After Vortex Breakdown[20]

1. left
2. right

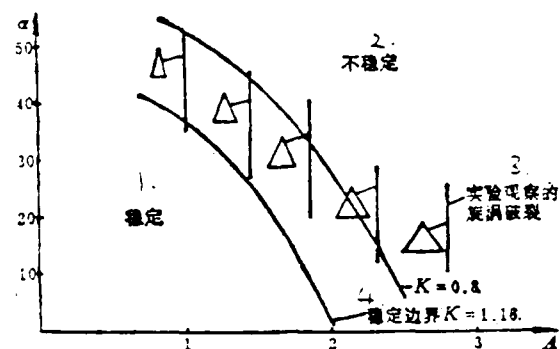


Figure 17. Theoretical Stability Boundary and Experimental Ranges of Vortex Breakdown in the (A, α) - plane[32]

1. stable
2. unstable
3. vortex breakdown observed experimentally
4. stability boundary

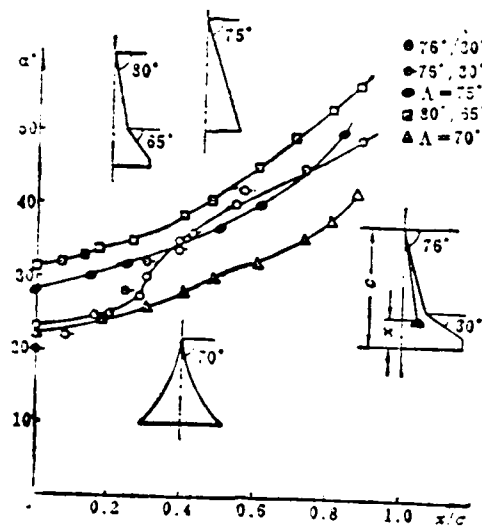


Figure 18. Comparison of Movement Pattern of Strake Wing to Slender Wing

IV. Controlled Separation and Vortex Interference

/9

A controlled separation is a separation which is capable of generating a free vortex layer and rolling into a stable vortex. It was pointed out in reference [36] that better aerodynamic designs might be obtained by creating and utilizing such separations. The concept will have a profound impact on aerodynamic research and design in the future. At this moment, the creation and utilization of controlled separation has already become one of the important issues in the aerodynamic design of fighter aircraft. Slender wings[37,50], strake wings[39-44], double delta wings[45,46], nearly coupled duck wing[38] and

spanwise blowing^[47-49] are actual examples in creating and utilizing controlled separations. It is obvious that the key is to create and maintain a stable concentrated vortex on the wing surface within a range of large attack angles. Based on Figure 11 we know that this can be done by using a sharp leading edge delta (or slender) wing with a large sweepback, such as the Concord wing. However, due to the requirements in subsonic and transonic performance, some aircraft must have medium sweepback and medium aspect ratio wings. It is impossible to create a stable concentrated vortex by itself. At large angles of attack, it can only create unsteady separated flows such as bursting vortex, spiral flow and reversed flow. To this end, we can add a large sweepback strake to its front end to form a strake wing (such as F-16 and F-18 wings). In addition to the direct contribution of the strake vortex (a stable concentrated vortex), the favorable interference of the strake vortex on the external flow field also has an important effect on the significant improvement in performance of strake wing at large attack angles^[43,44]. We can also see that controlled separation is closely related to vortex interference^[51].

The following is a discussion on the interferences on the wing, including the interferences between a concentrated vortex and other types of separated flows as well as the mutual interferences among vortices. Due to vortex interference, the types of separated flows may change. The stability of vortex may also vary. For instance, a strake vortex can essentially convert

a reversed flow or spiral flow on the wing to a bursting vortex to move the breakdown point of the bursting vortex downstream. It may even turn a bursting vortex into a steady concentrated vortex (provided that the strake vortex is strong enough). Based on Figure 19 we can see that when the angle of attack is 14° the vortex breakdown point on the basic wing is near the apex of the wing. A reversed flow occurs on the surface. The effect of the strake vortex, however, is to move the external wing vortex breakdown point downstream. It seems that this is primarily due to the fact that the spanwise component of the external wing flow velocity is increased because of the strake vortex which leads the external wing flow field toward the outside. This is beneficial in strengthening the stability of the vortex to delay the breakdown.

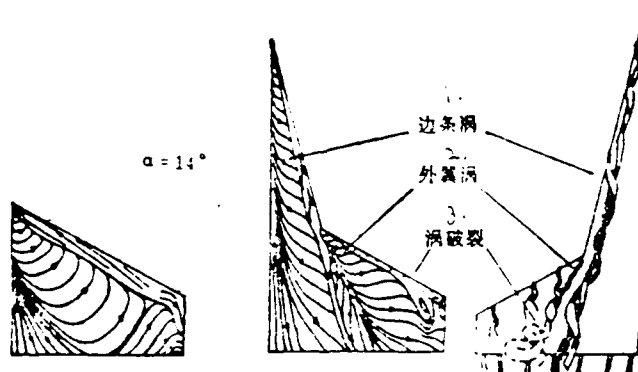


Figure 19. Flow Patterns on 30° Sweep Wing and $76^\circ/30^\circ$ Strake Wing

1. strake vortex
2. external wing vortex
3. breakdown vortex

The mutual interaction of two vortices of the same direction of rotation will lead to displacement, coalescence and consolidation. Displacement means that the relative position is becoming closer or changed. Coalescence means that the two may coalesce in a spiral form around each other. The specific form depends on the relative intensity of the two vortices. Consolidation means that the nuclei of the two vortices are mingled together. In this case, these two vortex nuclei may become one. They also may exist individually. Whether two vortices of the same direction of rotation can coalesce depends on the distance, vortex intensity ratio, size and structure of the vortex nuclei, and the angle between the two vortices.

The coalescence of forward panel vortex and rear panel /10 vortex of a double delta wing is shown in Figure 20^[45]. First, a concentrated vortex is rolled up at the leading edge of each panel. With increasing angle of attack, the two vortices begin to coalesce and then consolidate. It is reflected on the surface flow pattern as the secondary separation lines of these two vortices coincide. The point of coincidence moves forward with increasing attack angle. Within the range of where the angle of attack is not large, it has already reached the inflection point. The coalescence of these two vortices has been observed in various wind tunnel and water tunnel experiments^[26]. Furthermore, it was verified by spatial flow field measurements^[46]. The coalescence of these two vortices strengthened the stability of the rear panel vortex, delaying its

breakdown. On a strake wing, the two vortices only get close to each other and no coalescence takes place. This is because the angle between these two vortices is very large. Furthermore, the outer panel vortex is a bursting vortex. Under the condition of spanwise leading edge jet^[48], the coalescence of the leading edge jet vortex and the outer panel vortex occurs, as shown in Figure 21.

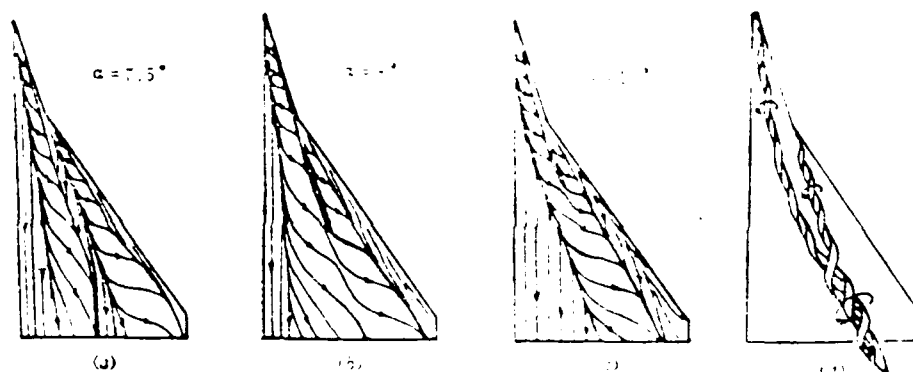


Figure 20. Mutual Interaction Between Front Panel and Rear Panel Vortices of 73°/57° Double Delta Wing

- (a), (b), (c) surface flow patterns
- (d) coalescence of two vortices

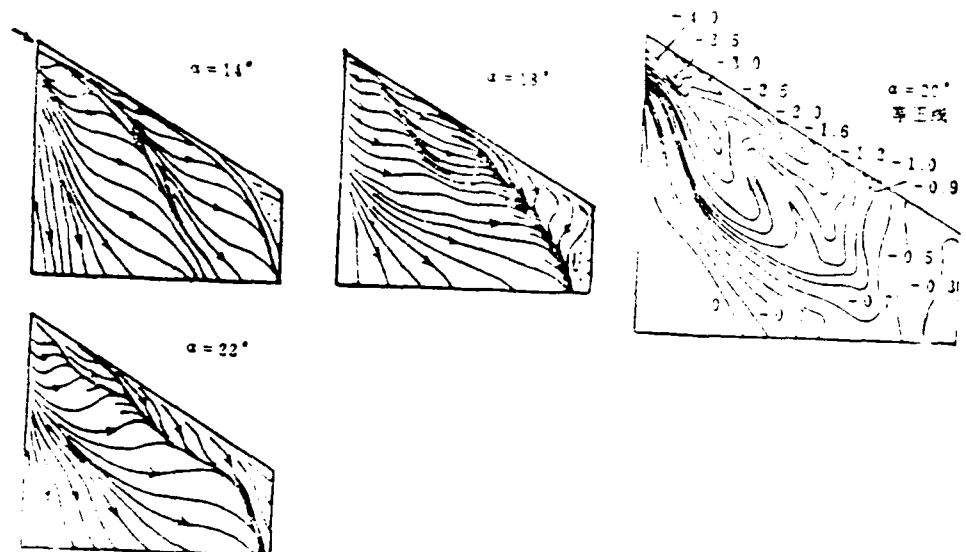


Figure 21. Mutual Interaction Between Jet Leading Edge Vortex and Outer Panel Vortex of Leading Edge Spanwise Blowing Wing

1. isobar

Comrades Xiong Shenwen, Gao Xiankun, Zhou Bochen, Qiu Chenwu, Liu Zhiyong, Deng Xueying and Liu Zhizhang also participated in the research of subjects related to this paper.

References

/11

- [1] Kachemann, D. and Weber, J., ZAMM, 45 (1965), Heft 7/8, Seits 457-474.
- [2] Progress in Aeron. Sci. Vol. 7, (1965).
- [3] Poisson, Quinton, P., Israel Journal of Techn. Vol. 16, (1978), pp. 97-131.
- [4] High Angle of Attack Aerodynamics AGARD CP-247, (1978).
- [5] Saffman, P.G., J. Fluid Mech. Vol. 106, (1981).

- [6] High Angle of Attack Aerodynamics AGARD LS-121, (1982).
- [7] Aerodynamics of Vortex Type Flows in Three-Dimensions, Conference Proceedings, AGARD CP-342, Jul. 1983.
- [8] Cornish, J.J. III, AIAA Paper 83-1812, (1983).
- [9] Maskell, E.C., RAE Report No. Aero. 2565, (1955).
- [10] Earnshaw, P.B. and Lawford, J.A., ARC R&M 3424, (1964).
- [11] Wei Zhonglei, Qiang Menchuan and Yang Maozhao, Chinese Journal of Aeronautics, Vol. 1, No. 1, (1965).
- [12] Smith, J.H.B., AGARD CP-168, No. 31, (1975).
- [13] Peake, D.J., AGARD LS-94, No. 5, 1978.
- [14] Werle, H., ONERA T.P. No. 1982-5, (1982).
- [15] Erickson, G.E., ICAS Paper 82-661, (1982).
- [16] Zhang Hanxing, Liu Linsheng and Yu Yichu, Chinese Journal of Mechanics, No. 3, 1983.
- [17] Legendre, R., Rech. Aeron. No. 54, Nov. (1956).
- [18] Oswatitsch, K., Boundary Layer Research edited by H. Gortler, IUTAM-Symposium, Freiburg, (1957).
- [19] Lighthill, M.J., Section II 2.6 and 2.7 of Laminar Boundary Layers, edited by L. Rosenhead, (1963).
- [20] Hunt, J.C.R., et al, J. Fluid Mech. Vol. 86, Part 1, (1968).
- [21] Tobak, M. and Peake, D.J., Ann. Rev. Fluid Mech. Vol. 14, (1982).
- [22] Legendre, R., La Recherche Aerospatiale, 1982-4.
- [23] Liu Moji, Su Wenhan, Liu Zhiyong and Deng Xueying, Technical Report of Beijing Institute of Aeronautics and

- Astronautics, BH-B1104, (1983).
- [24] Dallmann, U., AIAA Paper 83-1735, (1983).
 - [25] Lambourne, N.C. and Bryer, D.W., ARC R&M No. 3282, (1961).
 - [26] Wentz, W.H., Jr. et al, NASA CR-98737, (1968).
 - [27] Sarpkaya, T., J. Fluid Mech. Vol. 45, Part 3, (1971).
 - [28] Hall, M.G., Ann. Rev. Fluid Mech. Vol. 4, (1972).
 - [29] Lin Liangsheng, Zhong Guo Hweicheng, Journal of Japanese Society of Aeronautics and Astronautics, Vol. 20, No. 226, (1972).
 - [30] Leibovich, S., Ann. Rev. Fluid Mech. Vol. 10, (1978).
 - [31] Shi Xun-gang, Dissertation von der Fakultat fur Masschinenwesen de RWTH Aachen, West Germany, (1983).
 - [32] Wedmeyer, E.H., AGARD CP-247, No. 13, (1978).
 - [33] Naitai Maonan, Zhang Jinzheng and Zhongchun Jialong, Technical Report of Nanjing Institute of Aeronautics and Astronautics, 1555, (1982).
 - [34] Lin Bingqiu, Chinese Journal of Aerodynamics, No. 2, 1983.
 - [35] Zhou Bocheng, Technical Report of Beijing Institute of Aeronautics and Astronautics, BH-B852, (1982).
 - [36] Maskell, M.A. and Kuchemann, D., RAE TM No. Aero. 463, (1956).
 - [37] Wilde, M.G., Cormery, G., 11th Anglo-American Aeron. Conference, 193-331 (1969).
 - [38] Jiang Zhengbu, An Jiguang, Chen Zhengcai, Bei Xizhen, Huang Guochuang, Liang Zhenhui and Xiang Yansun, Journal of the 7210 Institute, No. 1, 1977.

- [39] Henderson, W.P. and Huffman, J.K., NASA TN D-7099, (1972).
- [40] Staudacher, W., DGLR 73-71, (1973).
- [41] Qiu Chenhou and Chen Yingxue, Technical Report of Beijing Institute of Aeronautics and Astronautics, BH-B266, (1976).
- [42] Lamar, J.E., AIAA Paper 78-1201, (1978).
- [43] M.J. Liu, Z.Y. Lu, C.H. Qiu, W.H. Su, X.K. Gao, X.Y. Deng, S.W. Xiong, J. Aircraft Vol. 17, No. 5, (1980), (AIAA Paper 79-1877).
- [44] Liu Zhizhong, Liu Moji and Su Wenhan, Symposium of Technical Reports of Beijing Institute of Aeronautics and Astronautics, Vol. 5, (1982).
- [45] Xiang Shenwen, Deng Xueying, Liu Moji, Lu Zhiyong, Su Wenhan and Gao Xiankun, Symposia of Technical Reports of Beijing Institute of Aeronautics and Astronautics, Vol. 5, (1982).
- [46] Brennenstuhl, U. and Hummel, D., ICAS Paper 82-663, (1982).
- [47] Cornish, J.J., III, ICAS Paper 70-09, (1970).
- [48] Su Wenhan, Liu Mouji, Zhou Bocheng, Qiu Chenghao, Xiong Shanwen, ICAS Paper 82-662, (1982).
- [49] Staudacher, W., Laschka, B., Poisson-Quinton, Ph., Ledy, J.P., AGARD CP-247, No. 8, (1978).
- [50] Hummel, D., AGARD CP-247, No. 15, (1978).
- [51] Saffman, P.G., Baker, G.R., Ann. Rev. Fluid Mech., Vol.11, (1979).

Application of New Type of Pole Collocation Equations to
Determining Laws Controlling A Bi-input Multi-output System

/13

Nanjing Aeronautical Institute Lu Shuqun

Abstract

In this paper, pole collocation equations for a bi-input multi-output system are derived. They are different from those commonly used in form. A property of these equations is proved to be able to better control the accuracy of the collocation of each eigenvalue. Numerical examples showed that the accuracy of poles obtained by this method was significantly better than that obtained by the "rank one controller".

I. Introduction

Pole collocation can be used to determine laws governing active flutter suppression^[1-3]. In the study of active flutter suppression of YF-17, in particular, the control laws were determined by the least square method (which is also based on pole collocation). Furthermore, it was successfully verified in wind tunnel experiments^[4]. This shows that pole collocation is a simple, practical and effective method.

The pole collocation method, however, still has some problems when used to determine the control laws for a bi-input multi-output system.

1. Under the condition that the feedback is not completely available, how can we collocate the eigenvalues which have a determining effect on the stability of the system, to the extent possible, according to the projected requirement? Presently, methods mostly used a polynomial s formed by eigenvalues. Then, the coefficients of the polynomials are fitted. However, each coefficient is related to all the eigenvalues. Eigenvalues with large modulus often have a determining effect. The modulus of an unstable eigenvalue, however, is not necessarily large. Hence, there is a considerable error in its collocation.

2. How can we better determine the control laws? The "rank one controller" can be used to determine the control laws for a bi-input multi-output system^[3]. However, it is required to be proportional to the feedback coefficient of the two inputs. Consequently, its effectiveness as a multi-output control system is affected.

In this paper, the eigenvectors of the matrix of the system are used to establish the collocation equations for each pole. Furthermore, the property of the equations is verified. This property is used to improve the accuracy in controlling the collocation of every pole.

A two-dimensional airplane wing with front and rear control surfaces was used as an example to perform a numerical calculation. The results showed that under the condition that the feedback is not completely available at the output, the

results obtained by this method are much better than those obtained by using a "rank one controller".

II. Pole Collocation Equation

1. Pole Collocation Equation

The equation of state, output equation and feedback equation of a closed system (See Figure 1) are

Manuscript received on July 28, 1983.

/14

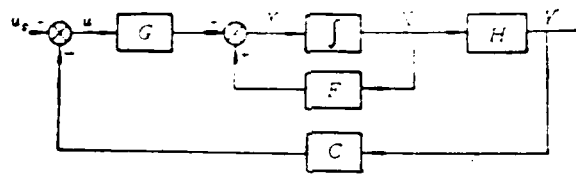


Figure 1. Block Diagram of the System

$$\begin{pmatrix} \dot{X} \\ Y \end{pmatrix} = \begin{pmatrix} F \\ H \end{pmatrix} X + \begin{pmatrix} G \\ 0 \end{pmatrix} u \quad (1)$$

$$\begin{pmatrix} \dot{X} \\ Y \end{pmatrix} = \begin{pmatrix} F \\ H \end{pmatrix} X + \begin{pmatrix} G \\ 0 \end{pmatrix} u \quad (2)$$

$$u = - \begin{pmatrix} C \end{pmatrix} Y \quad (3)$$

where $\{X\}$ is the state vector, $\{u\}$ is the control vector, $\{Y\}$ is the output vector, $[F]$ is the dynamic matrix of the open-loop system, $[G]$ is the control matrix. $[H]$ is the output matrix, and $[C]$ is the feedback matrix. The symbols in the parentheses underneath are the orders of the matrices.

Under the multi-output condition, $\{u\}$ must satisfy

$$\{u\} = -[C][H](s[I]-[F])^{-1}[G]\{u\} \quad (4)$$

The condition for $\{u\}$ to have a non-zero solution is

$$|[I] + [C][H](s[I]-[F])^{-1}[G]| = 0 \quad (5)$$

Under the bi-input condition, it can be expanded into

$$\begin{aligned} 1 - [C_1][H](s[I]-[F])^{-1}[G_1] - [C_2][H](s[I]-[F])^{-1}[G_2] &= 0 \\ [C_1][H](s[I]-[F])^{-1}[G_1] + [C_2][H](s[I]-[F])^{-1}[G_2] &= 0 \end{aligned} \quad (6)$$

In the above formula $[C_1]$ and $[C_2]$ are the first and two rows of $[C]$, and $\{G_1\}$ and $\{G_2\}$ are the first and second columns of $\{G\}$. $[F(s)] = (s[I]-[F])^{-1}$.

Let us assume that the eigenvalue matrix for an open-loop system is $[\Lambda]$. The left and right eigenvectors are $[Q]$ and $[P]$. Then

$$[F] = [P][\Lambda][Q] \quad (7)$$

$$[Q] = [P]^{-1} \quad (8)$$

$$[\bar{F}(s)] = [P](s[I]-[\Lambda])^{-1}[Q] \quad (9)$$

In this paper, $[P]$ and $[Q]$ are chosen to be complex matrices and $[\Lambda]$ is the corresponding complex diagonal matrix.

Thus, the pole collocation equations of a bi-input multi-output system are:

(1) If the allocated pole λ_k^* is not equal to any eigenvalue of $[F]$, then

$$\begin{aligned} 1 - [C_1][H](s[I]-[F])^{-1}[G_1] - [C_2][H](s[I]-[F])^{-1}[G_2] &= 0 \\ -[C_1][H](s[I]-[F])^{-1}[G_1] - [C_2][H](s[I]-[F])^{-1}[G_2] &= 0 \end{aligned} \quad (10)$$

In the above equation, the superscript T represents the transpose.

(2) If the allocated pole Λ_k^* equals an eigenvalue of [F], then

$$f(\Lambda_k^*) = [C_1]H[P_1] \Lambda_k^* + [C_2]H[P_2] \Lambda_k^* + G_1 + G_2 - \sum_{i=1}^n \frac{[C_1]H[P_1] \Lambda_k^* + [C_2]H[P_2] \Lambda_k^* + G_1 + G_2}{\Lambda_k^* - \Lambda_i} = 0 \quad (11)$$

$[P_j]$ is the j^{th} column of [P] and $[Q_j]$ is the j^{th} row of [Q]. $\Delta_i = \Lambda_k^* - \Lambda_i$, $[\bar{G}] = \{G_1\} \{G_2\} - \{G_2\} \{G_1\}$. /15

The derivation of equations (10) and (11) is in the appendix.

2. Property of Pole Allocation Equation (11)

If the pole Λ_k^* collocated is equal to an eigenvalue of Λ_j , and if the pole of the corresponding closed-loop system obtained is $\bar{\Lambda}_k$, then there is a finite error $\Delta\Lambda_j$,

$$\bar{\Lambda}_k - \Lambda_k^* = \Delta\Lambda_j = \Delta\alpha_j + i\Delta\omega_j \quad (12)$$

then

$$f(\bar{\Lambda}_k) \approx -\Delta\Lambda_j = -(\Delta\alpha_j + i\Delta\omega_j) \quad (13)$$

The expression for $f(\bar{\Lambda}_k)$ is equation (11) and only $\bar{\Lambda}_k$ is used to replace Λ_k^* . Its proof is shown in the appendix.

Equation (11) is weighted based on this property to improve the accuracy because when all the feedback is not available at the output the least square method is required to solve the problem. The modulus of the eigenvalue of $[F]$, however, may be very high. Thus, if not weighted, the errors of some eigenvalues of small modulus are often high. The real part of the instability eigenvalue, however, is usually not very large. Hence, the accuracy of the eigenvalue of most concern cannot be ensured.

Equation (11) can be weighted by using this property. For instance, the real and imaginary part can be weighted by $1/\omega_j$ and $1/\alpha_j$, respectively. This requires that the sum of the squares of the relative errors of their real and imaginary part be minimized. Thus, the accuracy of each root is appropriately assured.

It should be pointed out here that it is generally required that the original stable eigenvalues remain unchanged under a given design when poles are collocated. Therefore, the pole allocation equation usually has the same form as that of equation (11). In addition, it has been demonstrated by calculation that the above weighted method remains effective even when the poles allocated are not equal to the original eigenvalues, but the relative change is not very large (such as $\pm 10\%$).

As for the pole collocation equation (10), it is possible to determine whether it needs to be weighted based on the results.

If the unstable eigenvalue is $\alpha \pm i\omega$, then it is required to be allocated as $-\alpha \pm i\omega$. Then, the absolute error of the real part of the equation is equal to $2\alpha \Delta\alpha_0$. With regard to the two examples in this paper, α is larger than 1, which indicates that the weighted factor is larger than 1 for this error. Due to the fact that this eigenvalue affects stability, a larger weighted factor should be chosen to ensure its accuracy.

The pole collocation equations and properties derived above are also valid for a single input system. The specific form, however, is slightly different.

III. Examples

The Control Law for the active flutter suppression of a two-dimensional wing with front and rear control surfaces is calculated. The two-dimensional wing is shown in Figure 2. Its parameters are

$$\begin{aligned} x_0 &= 0.2, \quad x_3 = x_4 = 0.0125 \\ r_0^2 &= 0.25, \quad r_3^2 = r_4^2 = 0.00625 \\ c &= 0.6, \quad d = -0.6, \quad a = -0.4 \\ \omega_0 &= 500 \text{ rad/s}, \quad \omega_3 = 1000 \text{ rad/s}, \quad \omega_4 = \omega_5 = 2000 \text{ rad/s} \\ \zeta_0 &= \zeta_3 = 0.1, \quad b = 1, \quad \frac{m_l}{\pi \rho b^3} = 40 \end{aligned} \quad (A)$$

The meaning of these symbols are shown in reference [5].

When there is no control, the flutter velocity of the two-dimensional wing is $V_F = 290 \text{ m/s}$.

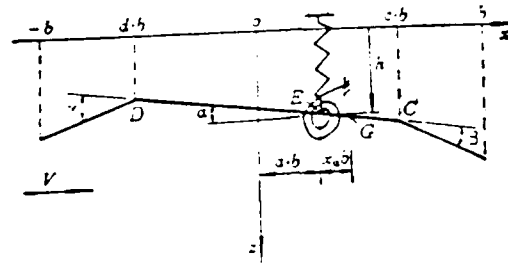


Figure 2. Two-dimensional wing

Let us assume the designed velocity is $V = 320\text{m/s}$. It is required that the stable eigenvalues obtained without control remain unchanged and the real part of any unstable eigenvalue has an opposite sign under this condition. When h, α, \dot{h} and α' are the output parameters, the control law is

$$[C] = \begin{bmatrix} -1.1247 & 0.3746 & -0.02330 & -0.002232 \\ -1.3350 & -0.4302 & 0.01417 & 0.005907 \end{bmatrix}$$

According to the design, the unstable eigenvalue is required to be collocated to be $-8.324 \pm 69.173 i$. In reality, it is collocated to be $-8.089 \pm 68.631 i$. The error of the real part is only 2.8%. The error for the remaining stable eigenvalues are generally less than 5%. In some individual cases, it reaches 14.4%.

The open-loop and closed-loop root locus diagram is shown in Figure 3. Its closed-loop flutter velocity is $V_F = 351.2\text{m/s}$.

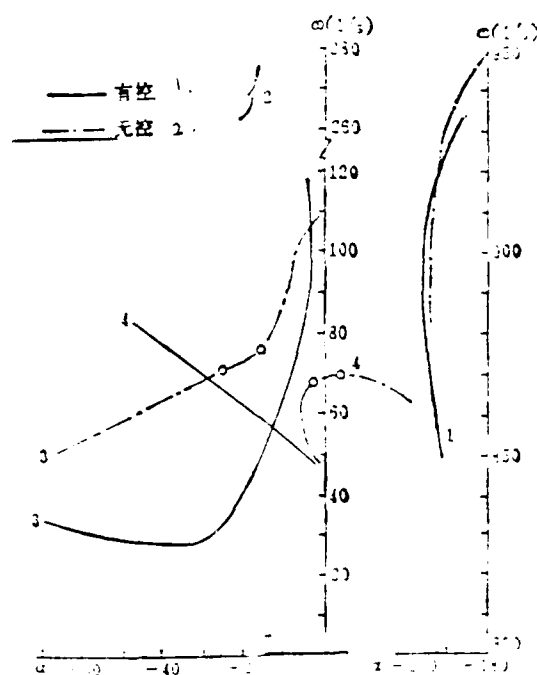


Figure 3. Open-loop and Closed-loop Root Locus Diagram of Example 1

1. with control
2. without control

For example 2 in reference [3], the control law obtained by the method derived in this work is:

$$C = \begin{bmatrix} -0.04021 & -0.07996 & -0.003859 & -0.0002231 \\ -0.05574 & -0.1067 & -0.003095 & -0.002449 \end{bmatrix} \quad (A)$$

Based on the design, the unstable eigenvalue is required to be collocated to be $-1.851 \pm 60.375 i$ in both reference [3] and in this work. In reference [3], it was collocated to be $-0.545 \pm 59.341 i$. The error of the real part is 70.6%. In this work,

it is collocated to be $-1.764 \pm 60.312 i$. The real part is merely 4.7%. The maximum error for the remaining stable eigenvalues is 6.5% (and in reference [3] it was 3.9%). Due to the fact that the unstable eigenvalue has a large impact on the phase and gain tolerance, the results obtained in this work showed much improvement over those reported in reference [3].

The closed-loop flutter velocity, however, was 333m/s in all cases because another branch showed signs of instability. The root locus diagram of some main branches is shown in Figure 4.

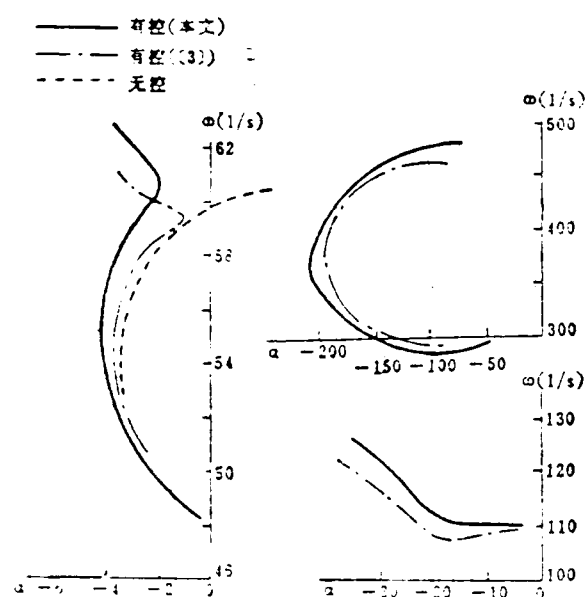


Figure 4. The Root Locus Diagram of Some Main Branches of Example 2

1. under control (this work)
2. under control ([3])
3. no control

IV. Conclusions

1. Each pole collocation equation derived in this paper corresponds to the real or imaginary part of each pole. In particular, the equations derived in this paper can be weighted so that the relative error of each pole would not be too different. This feature ensures the accuracy of the eigenvalue which is of most concern. Besides, in the method used in this work, unlike the "rank one controller" which puts constraints on the feedback coefficients, we can change all the feedback coefficients arbitrarily. This also makes it easier to collocate the poles. The results obtained with examples showed that the control law derived from this method are much more improved than that obtained with the "rank one controller".

2. The pole collocation equations derived in this work and the characteristics can be used in single-input cases.

3. When the relative change between the required pole and the original pole is not too large, the property of the equation mentioned above is still approximately valid.

Appendix Derivation of the Pole Collocation Equations

Under bi-input situation, the conditions for $\{u\}$ to have a non-zero solution is equation (6). If the collocated pole Λ_k^* is not equal to the eigenvalue of $[F]$, then we can use $s = \Lambda_k^*$ to plug into equation (6). After expansion, we get

$$\begin{aligned} 1 - [C_1][H_1][F]\Lambda_k^* - [G_1] - [C_2][H_2][F]\Lambda_k^* - [G_2] \\ - [C_1][H_2][F]\Lambda_k^* - [G_1][G_2] - [G_2][G_1] - [F]\Lambda_k^* - [C_1][H_1][F]\Lambda_k^* = 0 \end{aligned} \quad (A1)$$

/18

where

$$[\bar{F}(\Lambda_k^*)] = [P][\Lambda_k^*[I] - [A]]^{-1}[Q] \quad (A2)$$

Equation (A1) is equation (10).

If the collocated pole Λ_k^* is equal to an eigenvalue Λ_j of $[F]$, then $(\Lambda_k^*[I] - [A])^{-1}$ is singular which needs to be treated.

$$\begin{aligned} (s[I] - [F])^{-1} &= \sum_{i=1}^n \frac{(P_i)(Q_i)}{s - \Lambda_i} \\ &= P_n(Q_n) \frac{1}{s - \Lambda_n} + \sum_{i=1}^{n-1} \frac{(P_i)(Q_i)}{s - \Lambda_i} \end{aligned} \quad (A3)$$

If we note

$$[H][F][Q] = [H]Q \quad (A4)$$

Then equation (A3) can be plugged into equation (7). After we expand it and multiply it with $s - \Lambda_j$, we get

$$\begin{aligned} (s - \Lambda_j + [C_1][HQ])(G_1) &= \sum_{i=1, i \neq j}^n \frac{[C_1][HQ](G_1)}{s - \Lambda_i} \frac{s - \Lambda_j}{s - \Lambda_i} \\ &+ [C_2][HQ](G_2) + \sum_{i=1, i \neq j}^n \frac{[C_2][HQ](G_2)}{s - \Lambda_i} \frac{s - \Lambda_j}{s - \Lambda_i} - \left([C_1][HQ](G_1) \right. \\ &+ \sum_{i=1, i \neq j}^n \frac{[C_1][HQ](G_1)}{s - \Lambda_i} \left. \frac{s - \Lambda_j}{s - \Lambda_i} \right) \frac{1}{s - \Lambda_j} \\ &+ \sum_{i=1, i \neq j}^n \frac{[C_2][HQ](G_2)}{s - \Lambda_i} \frac{s - \Lambda_j}{s - \Lambda_i} \frac{1}{s - \Lambda_j} \\ &+ \sum_{i=1, i \neq j}^n \frac{[C_1][HQ](G_1)}{s - \Lambda_i} \frac{1}{s - \Lambda_j} \\ &+ \sum_{i=1, i \neq j}^n \frac{[C_2][HQ](G_2)}{s - \Lambda_i} \frac{1}{s - \Lambda_j} \end{aligned} \quad (A5)$$

When $s - \lambda_j$ is a small quantity, two terms in the above formula are of the order of $(s - \lambda_j)^{-1}$.

$$I_1 = [C_1, H, P, Q, G, P, H, P, Q, G] \cdot \frac{1}{s - \lambda_j} \quad (A6)$$

$$I_2 = [C_1, H, P, Q, G, P, H, P, Q, G] \cdot \frac{1}{s - \lambda_j} \quad (A7)$$

But, $I_1 - I_2 = 0$. Let $s - \lambda_j \rightarrow 0$. Thus, we can omit terms proportional to $s - \lambda_j$ and obtain the following equation.

$$\begin{aligned} I_1 - I_2 &= [C_1, H, P, Q, G, P, H, P, Q, G] \cdot \frac{1}{s - \lambda_j} \\ &= \sum_{i=1}^n [C_1, H, P, Q, G, P, H, P, Q, G] \cdot \frac{1}{s - \lambda_j} \\ &= [C_1, H, P, Q, G, P, H, P, Q, G] \cdot \frac{1}{s - \lambda_j} \\ &= \sum_{i=1}^n [C_1, H, P, Q, G, P, H, P, Q, G] \cdot \frac{1}{s - \lambda_j} \\ &= [C_1, H, P, Q, G, P, H, P, Q, G] \cdot \frac{1}{s - \lambda_j} = 0 \end{aligned} \quad (A8)$$

Equation (A8) is equation (11) in the text. / 19

In the following, we will prove the property of equation (A8); i.e., if the closed-loop eigenvalue obtained $\bar{\lambda}_k^*$ is not equal to λ_k^* , then there is a not so large error.

$$\lambda_k^* = \lambda_k + \epsilon \lambda_k = \bar{\lambda}_k^* \quad (A9)$$

i.e.,

$$f(\lambda_k^*) \approx -\lambda_k^* = -(\lambda_k + \epsilon \lambda_k) \quad (A10)$$

However, we still start from equation (A5) and substitute $s = \bar{\lambda}_k^*$ into equation (A5). Furthermore, we note that $\lambda_j = \lambda_k^*$, i.e., $s - \lambda_j = \bar{\lambda}_k^* - \lambda_k^* = \epsilon$. Then

$$\begin{aligned}
\Delta\lambda &= [C_1] HQD(G) + [C_2] HQD(G) + \sum_{i=1, i \neq j}^n [C_i] HQD(G) \\
&+ [C_{n+1}] HQD(G) - \frac{\Delta\lambda}{\lambda_k - \lambda_j} (I_1 - I_2) - \sum_{i=1, i \neq j}^n \frac{\Delta\lambda}{\lambda_k - \lambda_i} HQD(G) \\
&- \frac{\Delta\lambda}{\lambda_k - \lambda_1} HQD(G) - \sum_{i=1, i \neq j}^n \frac{\Delta\lambda}{\lambda_k - \lambda_i} HQD(G) \\
&- HQD(G) - HQD(G) - C_0 \frac{\Delta\lambda}{\lambda_k - \lambda_j} \\
&- \sum_{i=1, i \neq j}^n \sum_{l=1, l \neq j}^n ([C_l] HQD(G)[G_l] - [G_l][G_l] HQD(G)) \\
&\frac{\Delta\lambda}{\lambda_k - \lambda_j} \frac{\Delta\lambda}{\lambda_k - \lambda_l} = 0
\end{aligned} \tag{A11}$$

It is proven before that $I_1 - I_2 = 0$. In addition, $\Delta\lambda_j$ is a small quantity. Furthermore, in an elastic aerodynamic system, the two eigenvalues are generally not very close. This means that $|\lambda_k^* - \lambda_i|$ is relatively large. Therefore, $\frac{\Delta\lambda_j}{\lambda_k - \lambda_j} \ll \Delta\lambda_j$. Thus, it can be neglected. Similarly, $\frac{\Delta\lambda_j}{(\lambda_k - \lambda_1)(\lambda_k - \lambda_l)}$ terms can also be omitted. Thus, the remaining terms are

$$\Delta\lambda + f(\lambda_k) \approx 0$$

Therefore, (A12)

$$f(\lambda_k) \approx -\Delta\lambda_j = -(\Delta\alpha_j + i\Delta\omega_j)$$

The examples we calculated showed that this property exists.

References

- [1] Karpel, M., Design for Flutter Suppression and Gust Alleviation Using State-Space Aeroelastic Modeling, AIAA Paper 80-0766, May, (1980).
- [2] Li Chenyi (translator's note: rest in Japanese).
- [3] Gu Zhongquan, Determination of Control Law for Active Flutter Suppression of a Two-dimensional Wing, Journal of Nanjing Aeronautical Institute, Vol. 2, 1982, p. 36-46.
- [4] Hwang, C., Johnson, E.H., Mills, G.R., Noll, T.E., and Farmer, M.G., Wind Tunnel Test of a Fighter Aircraft Wing/Store Flutter Suppression System-An International Effort, AGARD Report No. 689.
- [5] Lu Shuquen, Using Pole Collocation to Determine the Control Law of a Bi-input Multi-output System and Its Application in Active Flutter Suppression Research, Technical Report No. 1684 of Nanjing Aeronautical Institute, (1983), 7.

QUICK GEOMETRY GENERATION AND SURFACE MESH PARTITION FOR ARBITRARY 3-D BODIES

Tang, Zigang, Li Anqui, Cao Shujiang
(Chengdu Aeronautical Company)

ABSTRACT

Abstract

A method of the surface fitting of three-dimensional bodies is presented in this paper. The longitudinal lofting curves are a chain of conics generated by the least square fitting, whereas cross-sectional curves are hybrid blended conics which contain circular arcs, elliptic arcs and straight lines. A FORTRAN program involving the computer graphics on the SIEMENS 7.760 computer has been written. The program is capable of quick and handy generation of the complicated configuration of 3-D bodies and surface meshes required in the aerodynamic influence coefficient method. The applicability and validity are verified by some numerical examples. Further development of the program enables it to be a graphic master dimensional system for computer aided design.

I. INTRODUCTION

Generation of surface meshes is necessary in carrying out aerodynamic analysis or stress analysis of an aircraft [1]. In these analyses, a mathematical model of the surface configuration of the aircraft is generated first and then the geometric characteristics of the meshes are calculated.

In the last 20 years, various mathematical models have been developed for the application in CAD/CAM. However, as indicated in reference [2], several models are inconvenient in application or may create unexpected surface distortion or bulge.

In the early stage of the numerical aerodynamic calculation developed in foreign countries, the interpolation technique has been used for both longitudinal and the cross-sectional directions or for the longitudinal direction only coupled with the analytical technique [3] for the cross-sectional direction to generate the body configuration. The requirement of large amounts of data input and poor accuracy of fitting are the problems. In the 70's F. R. deJarnette has proposed the use of a chain of conics generated by the least square fitting for the cross-sections, whereas the use of longitudinal lofting curves of conics fit the surface of the 3-D body [2]. Since the analytical calculations are used for both longitudinal and crosswise, it has eliminated the problem of interpolation. This method can be used to generate complicated configuration. However, since the longitudinal calculation and the crosswise calculation should be carried out alternatively, the connections of the longitudinal lofting curve sections are not smooth. Other programs developed by S. H. Stack and others [4] for arbitrary 3-D bodies are based on the assumption that the lofting curves are formed by a chain of elliptical curves in both longitudinal and cross-sectional directions. This numerical model is simple, integrated and can quickly generate the configuration of a complicated body. It has been applied in the development of the X-24 aircraft. The main problem of this model is that it needs to input the "control points for the slopes" which are difficult to be determined and, therefore, calls for large amounts of data inputs and calculations. In the 70's, a method was developed in our country using the technique with generating lines and center lines and has been applied in various aircraft design. However, this method is unable to generate complicated configurations, such as a combined body with wings attached. Advanced numerical models are needed in the modern aircraft design and aerodynamic analyses.

We have developed a method to fit the surface of three dimensional bodies based on references [2,4]. The method guarantees the continuity and is simple, quick and easy to be used for local surface modification and mesh partitions. In this method, the

longitudinal lofting curves are a chain of conics generated by the least square fitting, whereas the cross-sectional curves are obtained by hybrid blending circular arcs, elliptic arcs and straight lines. After the configuration of the 3-D body is generated, the geometric characteristics of the meshes are then calculated as needed by the aerodynamic influence coefficient method [5].

In addition, for the convenience of analysis and checking, a computer graphic program is included in the method. The program can be used to plot the 3-D figures, side views, the longitudinal lofting curves and the cross-sectional curves.

II. ANALYSIS

In body design, several points, control lines and tangential data should be determined according to the design requirements. After the body is fixed, the configuration can be determined by the theoretical diagram and the three side views or by the measurements of the real object. We have chosen several reference points on a group of the cross-sectional contour, such as top apex, bottom apex, intersection points and widest points, etc., as the bases to generate the configuration of the body. Since the cross-section of the body is symmetric, it is necessary to fit only half of the configuration. In our convention, the coordinates of the given points (data points) on cross sections are fed into the computer starting from the top apex and then to the points clockwise of the right half of the body. Since the configuration of the body is complicated, it is necessary to divide the body into several sections along the longitudinal direction. Each section has "similar" cross-sections which have the same number of data points and the same characteristics of curves (i.e., circles, elliptic arcs or straight lines). Several longitudinal lofting curves (space curves) can be obtained by feeding to the computer the consecutive data of the points on sequential cross-sections and a group of longitudinal information. The total number of

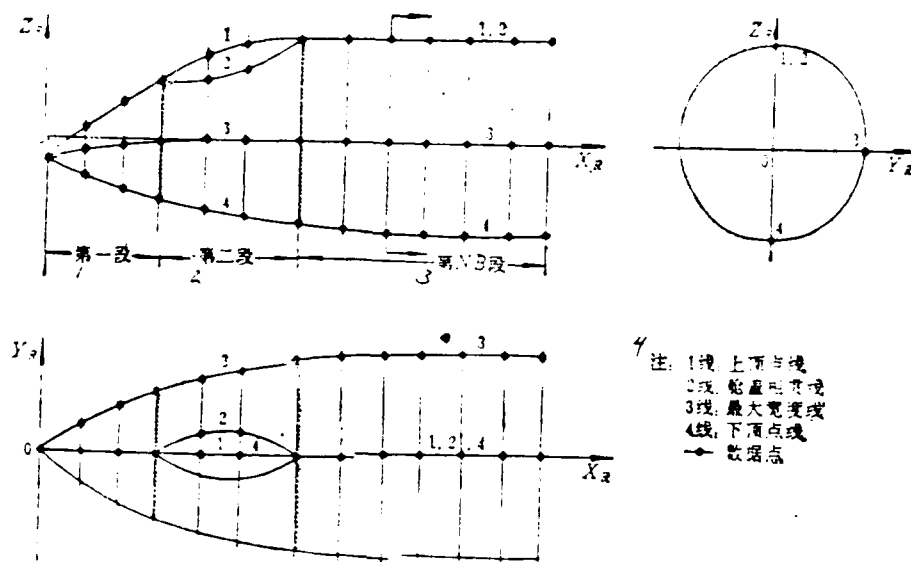
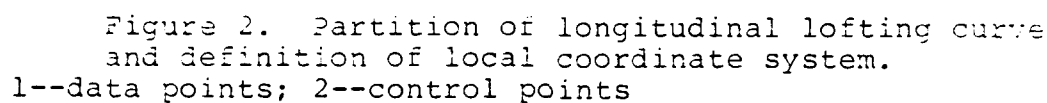


Figure 1. Reference coordinate system and longitudinal lofting curves

1--first section; 2--second section; 3--NB-th section;
4--NOTE: curve 1: curve at top apex; curve 2: canopy curve;
curve 3: curve at maximum width; 4: curve at bottom apex;
—o—data points

data points on each lofting curve is the same and any two curves may overlap (as shown in Figure 1). The least square fitting of a chain of conics is then carried out for the projected curves of each lofting curve on the $X_R Y_R$ and $X_R Z_R$ surfaces.

For example, data points $k = 1, 2, \dots, N_{k0}$ are set up on the front view projection curve of the longitudinal lofting curve. The control points $j = 1, 2, \dots, N+1$ can be determined according to the curvature of the projection curve. It is assumed that the control points coincide with the data points having the corresponding numbers K_1, K_2, \dots, K_{N+1} and the curve between two consecutive control points is conic. For simplifying the analysis, local coordinate systems, $jXYZ$ are used for each segment of the conic curve. The origin is set at the first control point of each segment of the curve. Z axis passes the first and the last control points, X axis is perpendicular to the Z axis and the y axis is



/31

Assuming the equation for the j-th segment of the conic curve on the local coordinate system is:

with the boundary conditions that the conic curve passes the first and the last control points and the consecutive segments of the conic curve are tangent to each other at the joined control point, equation (1) can be reduced to:

51

where the coefficients α_j , β_j and γ_j can be calculated from the data points in segment j [2]. With large amounts of data points, the following two equations can be obtained by least square fitting.

$$\sum_{i=1}^N a_{mi} A_{mi-1} - \sum_{i=1}^N a_{mi} C_{mi-1} = 0 \quad (3)$$

($m = 2, 3, \dots, N$)

and

$$\sum_{i=1}^N b_{mi} A_{mi-1} - b_{mi} C_m = 0 \quad (4)$$

($m = 1, 2, \dots, N$)

where $A = A_i = 0, 1, 2, \dots$ and b_{mi} are defined in reference [2] to be functions of a given data point. The coefficients C_1 , A_2 and C_j ($j = 2, 3, \dots, N$) of the conic equation (2) can be obtained by solving the above two equations. Let $A_1 = 1$, then the equations for each conic segment are fixed.

For solving equations (3) and (4), we have derived the following diagonal matrix.

$$\begin{array}{ccccccccc} H_{2,1} & H_{2,2} & H_{2,3} & & & & & & \\ H_{3,1} & H_{3,2} & H_{3,3} & H_{3,4} & H_{3,5} & & & & \\ H_{4,1} & H_{4,2} & H_{4,3} & H_{4,4} & H_{4,5} & & 0 & & \\ & H_{5,1} & H_{5,2} & H_{5,3} & H_{5,4} & H_{5,5} & & & \\ & & H_{6,1} & H_{6,2} & H_{6,3} & H_{6,4} & H_{6,5} & & \\ & & & H_{N-2,1} & H_{N-2,2} & H_{N-2,3} & H_{N-2,4} & H_{N-2,5} & \\ 0 & & & & H_{N-1,1} & H_{N-1,2} & H_{N-1,3} & H_{N-1,4} & \\ & & & & & H_{N,1} & H_{N,2} & H_{N,3} & \end{array} \begin{array}{c} A_2 \\ A_3 \\ A_4 \\ A_5 \\ \vdots \\ A_m \\ \vdots \\ A_{N-2} \\ A_{N-1} \\ A_N \end{array} = \begin{array}{c} -H_{2,1} \\ -H_{3,1} \\ 0 \\ 0 \\ \vdots \\ 0 \\ \vdots \\ 0 \\ 0 \\ 0 \end{array} \quad (5)$$

where

$$\begin{aligned} H_{m,1} &= a_{m,1} - \frac{b_{m-1,1}}{b_{m-1,4}} a_{m,4} \\ H_{m,2} &= a_{m,2} - \frac{b_{m-1,2}}{b_{m-1,4}} a_{m,4} - \frac{b_{m,1}}{b_{m,4}} a_{m,7} \\ H_{m,3} &= a_{m,3} - \frac{b_{m-1,3}}{b_{m-1,4}} a_{m,4} - \frac{b_{m,2}}{b_{m,4}} a_{m,7} - \frac{b_{m-1,1}}{b_{m-1,4}} a_{m,9} \\ H_{m,4} &= a_{m,4} - \frac{b_{m,1}}{b_{m,4}} a_{m,7} - \frac{b_{m-1,2}}{b_{m-1,4}} a_{m,9} \\ H_{m,5} &= a_{m,5} - \frac{b_{m-1,3}}{b_{m-1,4}} a_{m,9} \end{aligned} \quad (6)$$

($m = 2, 3, \dots, N$)

Analysis shows that the coefficient matrix of equation (5) is a symmetric matrix and the A_j ($j = 2, 3, \dots, N$) can be obtained from the matrix. The other coefficient C_j of equation (2) can be obtained from the following equation:

$$C_m = -\frac{1}{b_{m+1}} \sum_{i=1}^3 b_{m+1,i} A_{m-i+1} \quad (7)$$

$(m = 1, 2, \dots, N)$

So far, the analytic equations, with local coordinate system, of each conic segment of the front view projection of the longitudinal lofting curve are obtained. Similar fitting of the top view projection of the longitudinal lofting curve can be carried out. For the convenience in application, the conic equations under the local coordinate system can be transformed to the conic equations under the standard coordinate system.

However, if the fitted conic curve is a hyperbolic function, the curve in such segments can be assumed to be a straight line across two control points. That is

$$X = 0 \quad (8)$$

This assumption expanded the range of the least square fitting of a chain of conics proposed by reference [2] and produces longitudinal lofting curves which contain straight lines, break points and interruption points.

The following conditions should be reminded in carrying out the longitudinal curve fitting:

1. The distribution of the given data points should not be over scattering. Nonlinear segments should not be fitted as hyperbolic curves.

2. There should not be too many control points. The number should be less than $1/2 (N_k + 3)$. It is preferable having more than one data point to none between two adjoining control points. However, there should not be infinite numbers of data points between two adjoining conic segments.

3. It is favorable to have more data points in the first and the second conic segments. Otherwise, the fitting may fail because of poor accuracy in solving equation (5).

133

In summary, a satisfactory fitted longitudinal curve requires many modifications of the data points and large amounts of information. However, keeping the above three rules in mind, the fitting is quite easy to obtain. The cross-sectional fitting can be carried out when all the longitudinal lofting curves are obtained.

Assuming the coordinates of the characteristic point (Y_R, Z_R) on the cross-section at X_R are obtained by analyzing the longitudinal lofting curve, the cross-section can be found by fitting the curves between two adjoining control points with circular arcs, elliptic arcs and straight lines. Fitting with circular arcs or elliptic arcs only is limited in application. As shown in Figure 3, for a typical cross-section, the slope at $j = 4$ is not continuous and the slopes at the points $j = 1, 6$ and N_s are fixed (corresponding to the top apex, the widest point and the bottom apex), fitting with circular only cannot control the slopes at these characteristic points and cannot preserve the shape and the smoothness of the configuration. With elliptic fitting methods [4], the values of the slope at the characteristic points should be given or a "control point" should be added between two adjoining characteristic points. This increases significantly the amount of data and calculations. We have successfully solved this problem by using the blended method which contains circular arcs, elliptic arcs and straight lines.

In our fitting process, the coordinates and the horizontal information of the characteristic points are listed starting from the top apex to the next point clockwise. Partition points are set up at the inflection points. Each cross-section within the same geometric section of the body should have the same numbers of characteristic points, partition points and horizontal information. A geometric region is formed between two adjoining partition points and it contains several curve segments. The hybrid

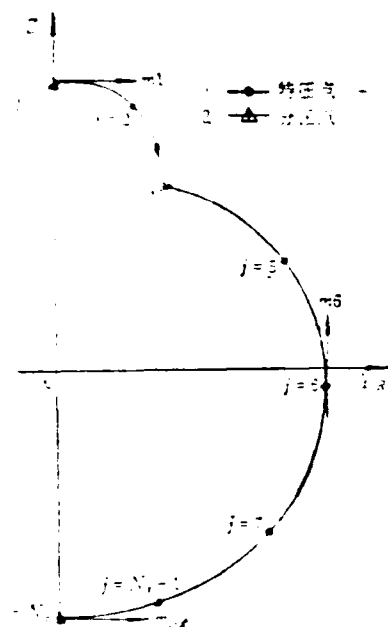


Figure 3. A typical schematic diagram of the cross-section fitting.

1-- characteristic point
2-- separation point

and blended calculations are carried out for each geometric region. As shown in Figure 3, the first region has three segments which are circular arcs, elliptic arcs and straight lines. The second region has N_4-4 segments. Because of the restriction of the slopes at $j = 6$ and $j = N_5$, all segments are circular arcs except the N_5-1 segment which is an elliptic arc. The calculation of the curves of the segments follows the order, $j = 1, 3, 2, 5, 4, 6, 7, \dots, N_5-1$. The order of calculation is determined by the position of the partition points and the slopes at the characteristic points. Such information can be easily obtained from the characteristics of the body configuration.

The equation of elliptic fitting can be obtained from reference [4]. A local coordinate system is used in this fitting which gives two coefficients in the elliptic equation. The elliptic equation can be obtained from the coordinates of the two end points of the segment to be fitted and the slopes at the two points or the control points. We have transformed the elliptic equation into the reference coordinate system for the convenience of calculation.

The reference coordinate system is used for the circular arc fitting. The radius and the position of the center are determined with three boundary conditions. Two types of boundary conditions have been used in our calculations, one with given coordinates of the two end points and the slope at one of the end points, the other with the coordinates of three adjoining points and the condition having the two circular arcs tangent to each other. We have developed the iteration equations of blending multiple circular arcs to determine the original circles based on the above two types of boundary conditions.

Two-point linear equations are used for straight line fitting

The mathematical model of hybrid blended conics containing circular arcs, elliptic arcs and straight lines, is simple and flexible in application. The model contains the pure circular arcs fitting and the pure elliptic arcs fitting as special cases. The model does not have the problem of incompatibility of two circular arcs or two elliptic arcs as that mentioned in reference [6]. However, many modifications of the information are needed to obtain a satisfactory horizontal fitting and to assure the smoothness of the configuration. Calculation shows that proper values of the slopes at the top apex, the widest point, the bottom apex and some other characteristic points on the cross-section can effectively assure the smoothness of the surface configuration. In addition, since the interaction between the longitudinal fitting and the horizontal fitting is weak, the configuration of the three-dimensional body can be easily generated with a good fitting of the longitudinal lofting curves and a reasonable control of the slopes at various points on the cross-section. /34

The current numerical model for generating the configuration of three-dimensional bodies has been applied in calculations of the subsonic speed surface elements. With given information of the longitudinal and horizontal partitions, the geometric characteristics of the surface meshes of the body can be calculated. We have divided the perimeter of the body into segments of equal arc length and the longitudinal direction by cosinoidal partition or equal spaces. This method of partition can provide uniform meshes and reasonable distribution of meshes, which gives better accuracy in numerical calculations of aerodynamics.

III. PROGRAM INTRODUCTION

The program was written in Fortran using SIEMENS7.760 computer. It contains four major parts including information treatment, longitudinal and horizontal mesh partition, calculation of the geometric characteristics of the surface meshes and computer plotting.

It has 64 modules and 6517 statements.

The user can input the limited information and the geometric data with the codes to form a data file. With the BS2000 operation system, the coefficients of the longitudinal and the horizontal conic equations and the geometric characteristics of the surface meshes can be quickly calculated. The latter includes the coordinates of the mesh points, odd points and the center points and parameters such as area, unit tangent vectors and unit normal vectors. The calculated results can be used as data base for aerodynamic calculations or other treatments. The interim results and the final results can be output in broad lines and the three projective views of the body, side view, longitudinal lofting curves and diagrams of cross-sections can be plotted using BENSON model 1320 plotter. The program has the following major characteristics:

1. The generality and the complexity of the three dimensional body as well as the simplicity and the flexibility of inputting data are considered in the program.

2. The program has considered the special characteristics of the BS2000 operation system. The computer operation is simple with reasonable utilization of memory buffer, file management and comments. The program can also be used in SIEMENS 7.738 computer.

3. The program has been designed with modules and is expandable and adaptable for future processing.

IV. EXAMPLES

Calculations of various bodies, including rotating body, schematic body, wing fuselage blended body and three types of real fuselage models, were carried out to demonstrate the effectiveness of our calculation technique. Two examples are discussed as follows:

Figure 4 shows the longitudinal lofting curve fitting, which includes 3/4 order hyperbolic curves, straight segments and break points. The deviations of the fitted values are within 0.5% of the accurate values. More accuracy can be obtained with further adjustment. The figure shows also that the lofting curves containing steps, straight line segments can be fitted accurately with proper selection of the control points.

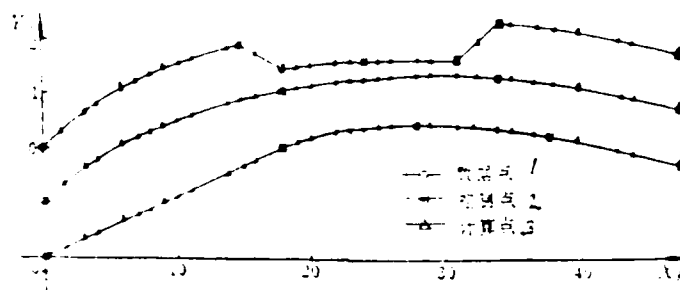


Figure 4. Longitudinal lofting curve fitting involving straight segments and break points.
1--data points; 2--control points; 3--calculated points

The configuration C in reference [7] is a wing-fuselage /35 blended body. The cross-sections are complicated and there are two vertical plates similar to abdominal fins at the tail. The preliminary result of fitting based on the three view drawing and 12 cross-sections given in reference [7] is shown in Figure 5. It shows that both longitudinal and horizontal fittings are reasonable and the two vertical plates are also visualized.

Additionally, we have fitted many wind tunnel models of real bodies including three dimensional bodies with air intakes on both sides, at abdominal region and at the nose. Satisfactory results with good smoothness and contour are obtained. Figure 6 shows the 3-D view and the 3 view drawing of the fuselage with two sided air intakes.

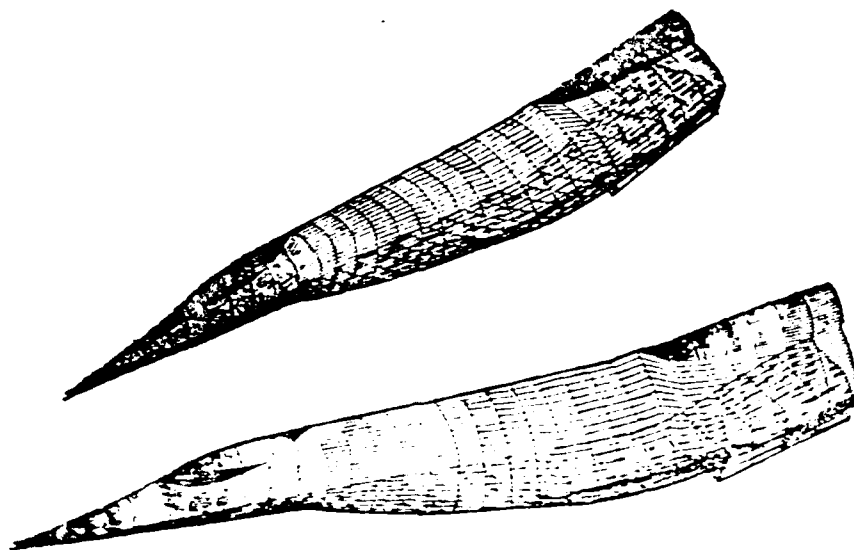


Figure 5. Fitting of wing-fuselage blended bodies.
(3-D view).

The figures of the fuselage with two-sided air intakes mentioned above are all plotted by computer. These figures, lofting curves and cross-sections can be used to check the quality of the fitting. The appearance of concave and convex areas can be easily eliminated by adjusting small amounts of the input data.

V. CONCLUSION

Conic curve fitting technique is widely applied in CAD because of its simplicity in mathematical definition and flexibility in various aspects. Our method of surface fitting of three-dimensional bodies can quickly generate the numerical model of the geometry of a complicated fuselage and the surface meshes for aerodynamic calculations. The major characteristics of this method are listed as follows.

1. This method is an integrated one-round model which can quickly generate the geometry. It can generate the configuration of more complicated bodies than the "block" type numerical model does.

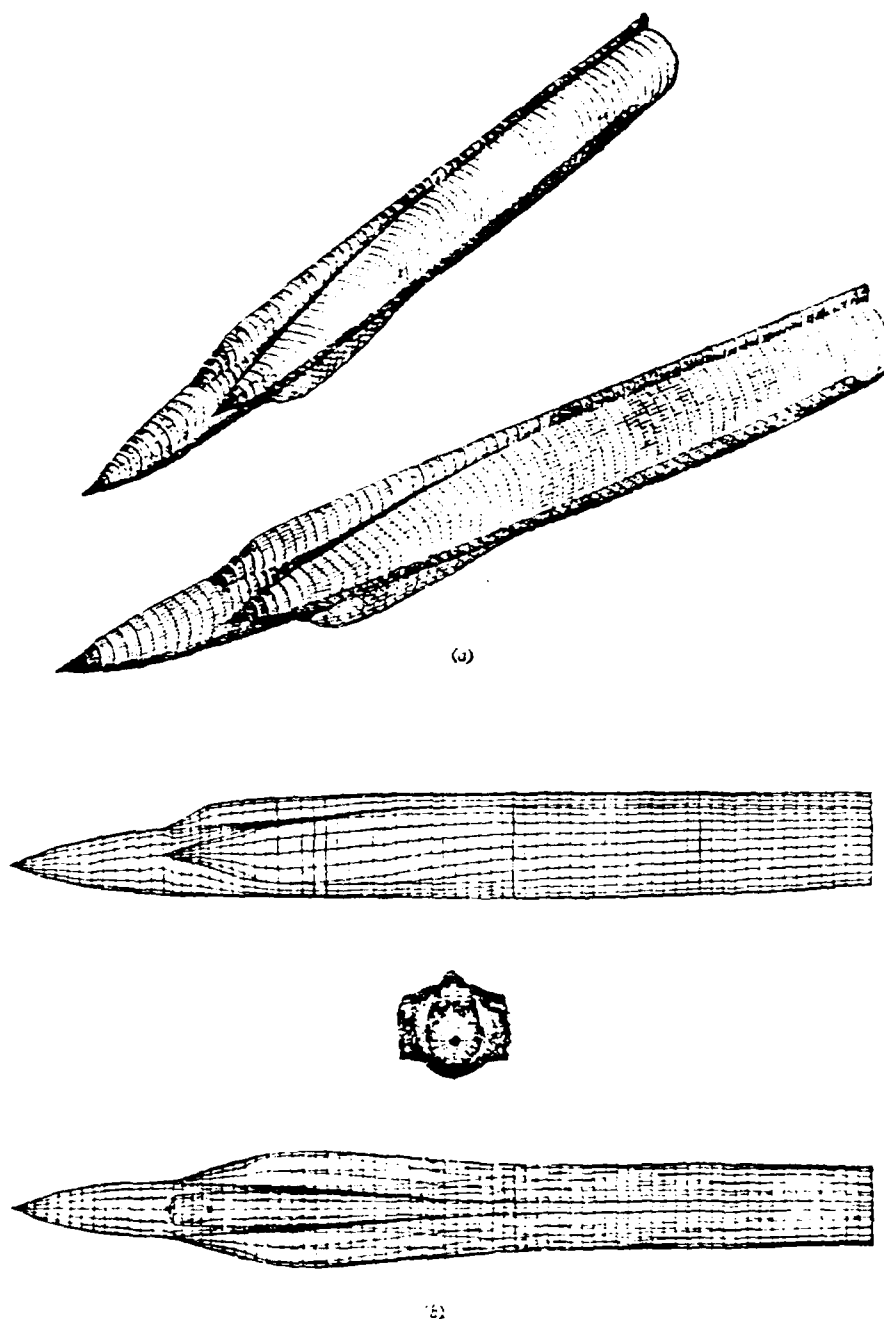


Figure 6. Fitting of fuselage with two-sided intakes
(a) 3-D view (b) view drawing

2. The least square fitting of the longitudinal conic chain has good adaptability. With proper selection of the control points, it can generate in one run the longitudinal lofting curves containing straight line segments, break points or interruption points. The shape of the body is well preserved without preprocessing of the data.

3. The blended calculation of circular arcs, elliptic arcs and straight lines of the cross-sectional curves can easily generate the cross-sections of a complicated body. The smoothness and the convex configuration of the surface geometry can be easily preserved with proper control of the slopes on the cross-sections.

4. The surface mesh partition along the perimeter is made with equal arc length which provides uniform size and distribution of the meshes and increases the accuracy of the subsonic vertex lattice method of calculation.

5. The program is simple in data set-up, convenience in operation and expandable. The program after expansion can be applied in preliminary design of the aircraft and the finite element analyses of the structure.

6. The quality of the fitting can be checked visually using the computer plotter. It can also be used to make regional modifications. The efficiency of fitting can be greatly improved by calculating on a graphic terminal. /37

Having the above characteristics, the method can be further developed for using as a main graphic system sizing in CAD.

REFERENCES

- [1] Workshop on Aircraft Surface Representation for Aerodynamic Computation, NASA TM-8170, (1980)
- [2] DeJarnette, F. R. etc., Surface Fitting Three-Dimensional Bodies, NASA SP 390, (1975), p. 447.
- [3] Applications of Computer Graphics in Engineering, NASA SP-390, (1975), p. 49
- [4] Stack, S. H., Edwards, C. L. W. and Small, W. J., GENPAK: An Arbitrary Aircraft Geometry Generator, NASA TP-1022, (1977)
- [5] Tang Ziqing, Li Anqui, Cao Shujiang: Quick Geometry Generation and Surface Mesh Partition for Fuselages, Discussion on CAD Techniques, Aeronautical Science Conference, 1983
- [6] Sylvan, H. C., Parametric Principles and Procedures for Computer Graphic Application, Lock-Heed Company, 1975
- [7] Blumstein, J. L., Application of Computer Theory and Hyperbolic Impact Methods to Three Dimensional Hypersonic Aerodynamics at Mach Numbers from 1.10 to 2.85, NASA TP-1039, 1977

NUMERICAL CALCULATION OF FLOW FIELD IN AFTERBURNER DIFFUSER OF TURBOFAN ENGINE

Chen Yiliang
(University of Science and Technology of China)

Sun Ci
(Shengyang Aeroengine Institute)

ABSTRACT

The flow field in the afterburner diffuser of a turbofan engine is calculated by the SIMPLE numerical method. The results are compared well with the measured data. The effects of the parameter distribution of the intake air flow on the flow field in the afterburner diffuser were studied. The flow field in the afterburner diffuser under different flight conditions and different rotating speed on the station were calculated.

1. INTRODUCTION

The flow field in the afterburner of the turbofan engine is complicated and is composed of both mixing and compressing processes. Since the diffuser has a larger expansion angle with a central cone, the flow may separate under certain working conditions. Elliptical differential equations are used to describe these types of flow at steady state conditions. The SIMPLE method developed by Patankar and others [1] is an effective tool to solve such differential equations. However, this method usually has the difficulty to get convergency. We have made a detailed analysis on the process and convergency of the SIMPLE technique and suggested a method to improve the convergency in reference [2]. In this paper, we have used the SIMPLE method to solve the flow field in the afterburner diffuser of the turbofan engine and studied the effects of the intake flow parameters on the flow field and the effect of flight conditions on the flow field in the diffuser.

II. MATHEMATICAL AND PHYSICAL MODEL

Figure 1 shows the geometric structure of the afterburner diffuser with parallel intakes of a typical turbofan engine. Both ends of the diffuser are circular tubes with a cone connected in between. There is a conic frustum at the center of the intake end. The intake cross-section of the solution was at the bottom edge of the annular confluent ring. The high temperature combustion gas from the main combustion chamber flows through the inner pass and the low temperature air flows through the outer passage. The ratio of the outer flow rate to the inner flow rate is the bypass ratio.

Assumptions for the calculations:

1. The combustion of the fuel is completed at high temperature and no chemical reaction is considered. Radiation heat and work done by viscosity are neglected.
2. The wall of the system is adiabatic and is nonpermeable for mass.
3. The temperature and the composition distributions of the outer and the inner flows at the inlet of the diffuser are homogeneous.
4. The flow field is axialsymmetric and no eddy flow.

Assuming the fuel in the main combustion chamber is C_8H_{16} and the ratio of fuel to air is q (less than the ratio of equivalent mixing), using the mass fraction of the combustion gas in the inner passage, f , as a parameter for the composition of the mixture, the mass fractions of CO_2 , H_2O , O_2 and N_2 in the flow field can be obtained by mass balance:

$$m_{O_2} = 352q / (1 + q) \quad (1)$$

$$m_{H_2O} = 144q / (1 + q) \quad (2)$$

$$m_{O_2} = (0.232 - 334q / 112) f + (1 + q) - 0.232(1 - f) \quad (3)$$

$$m_{H_2} = (1 - 0.232(1 - f) - (1 + q) - f) \quad (4)$$

With the above assumptions, the mass fraction of the combination gas in the inner passage, f , and the normalized enthalpy $H = (h - h_2) / (h_1 - h_2)$ have the same control equations and the same boundary conditions, and $f = H$ at any point within the flow field. Therefore, the stationary enthalpy at each point within the flow field is

$$h = f(h_1 - h_2) + h_2 \quad (5)$$

where h_1 and h_2 are the stationary enthalpies of the inner flow and outer flow at the inlet of the diffuser respectively.

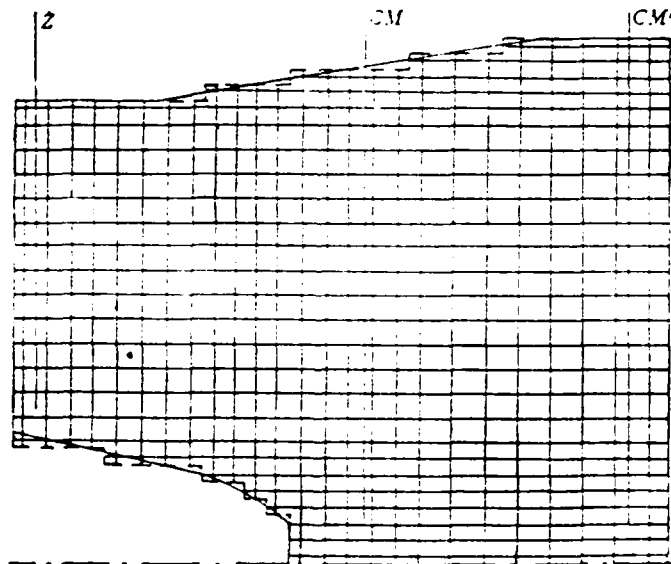


Figure 1. Grid and measuring sections

Considering the influence of turbulence on the flow process, we have used the mathematical model with dual equations for turbulence flow, which contains the turbulent energy, k , and the dissipation of the turbulent energy ϵ . The whole problem has six

equations, including axial velocity, radial velocity, continuity, mass fraction of the composition f , the quantities of the turbulence k and ϵ [3]. The general equation is

$$\frac{\partial}{\partial t} + \frac{1}{r} \frac{\partial}{\partial r} (r u \frac{\partial}{\partial x}) = \frac{\partial}{\partial x} (u \frac{\partial}{\partial x}) + \frac{1}{r} \frac{\partial}{\partial r} (r u \frac{\partial}{\partial r}) - S. \quad (6)$$

The definitions of various parameters, symbols $\frac{\partial}{\partial t}$, $\frac{\partial}{\partial x}$ and S , are shown in Table 1.

TABLE 1. Definition of parameters

1	2	3	4	5
1	2	3	4	5
2	3	4	5	6
3	4	5	6	7
4	5	6	7	8
5	6	7	8	9
6	7	8	9	10
7	8	9	10	11
8	9	10	11	12
9	10	11	12	13
10	11	12	13	14
11	12	13	14	15
12	13	14	15	16
13	14	15	16	17
14	15	16	17	18
15	16	17	18	19
16	17	18	19	20
17	18	19	20	21
18	19	20	21	22
19	20	21	22	23
20	21	22	23	24
21	22	23	24	25
22	23	24	25	26
23	24	25	26	27
24	25	26	27	28
25	26	27	28	29
26	27	28	29	30
27	28	29	30	31
28	29	30	31	32
29	30	31	32	33
30	31	32	33	34
31	32	33	34	35
32	33	34	35	36
33	34	35	36	37
34	35	36	37	38
35	36	37	38	39
36	37	38	39	40
37	38	39	40	41
38	39	40	41	42
39	40	41	42	43
40	41	42	43	44
41	42	43	44	45
42	43	44	45	46
43	44	45	46	47
44	45	46	47	48
45	46	47	48	49
46	47	48	49	50
47	48	49	50	51
48	49	50	51	52
49	50	51	52	53
50	51	52	53	54
51	52	53	54	55
52	53	54	55	56
53	54	55	56	57
54	55	56	57	58
55	56	57	58	59
56	57	58	59	60
57	58	59	60	61
58	59	60	61	62
59	60	61	62	63
60	61	62	63	64
61	62	63	64	65
62	63	64	65	66
63	64	65	66	67
64	65	66	67	68
65	66	67	68	69
66	67	68	69	70
67	68	69	70	71
68	69	70	71	72
69	70	71	72	73
70	71	72	73	74
71	72	73	74	75
72	73	74	75	76
73	74	75	76	77
74	75	76	77	78
75	76	77	78	79
76	77	78	79	80
77	78	79	80	81
78	79	80	81	82
79	80	81	82	83
80	81	82	83	84
81	82	83	84	85
82	83	84	85	86
83	84	85	86	87
84	85	86	87	88
85	86	87	88	89
86	87	88	89	90
87	88	89	90	91
88	89	90	91	92
89	90	91	92	93
90	91	92	93	94
91	92	93	94	95
92	93	94	95	96
93	94	95	96	97
94	95	96	97	98
95	96	97	98	99
96	97	98	99	100

1--equation; 2--continuity equation; 3--axial momentum; 4--radial momentum; 5--composition mass fraction; 6--turbulent energy; 7--kinetic energy dissipation

The increase of the kinetic energy of the turbulence is given by

$$G_k = \mu_t \left[2 \left(\frac{\partial u}{\partial x} \right)^2 + \left(\frac{\partial v}{\partial r} \right)^2 + \left(\frac{v}{r} \right)^2 + \left(\frac{\partial v}{\partial x} + \frac{\partial u}{\partial r} \right)^2 \right] \quad (7)$$

Neglecting the influence of the viscosity of laminar flow, the effective viscosity is given by $\mu = \mu_t = 0.09 \rho k^2 / \epsilon$. The values of the constants in the equations are $\sigma_1 = 0.09$, $\sigma_2 = 1.0$, $\sigma_3 = 1.3$, $c_1 = 1.49$, $c_2 = 1.92$.

III. BOUNDARY CONDITIONS

The number of grid points for the calculation is 27x28. Since the profiles of the outer shell and the central cone are broken lines or curves, we have replaced them with a group of lines with small steps for convenience and left the nodes for storing velocity on the step lines (Figure 1). The SIMPLE

method for solving the equations and the technique to obtain convergence are reported in references [1] and [2].

The boundary conditions should be given for solving the elliptical partial differential equation. Under subsonic flow condition, the downstream flow will affect the upstream flow. Therefore, the boundary conditions at the inlet and outlet cannot be defined. However, the influence of the downstream flow on the upstream flow can be neglected if the cross-sections of the inlet and outlet are selected at the points without backflow and the velocity of the down flow is very large. On the cross-sections of such inlet and outlet, local hyperbolic curves can be assumed. In our calculation, the values and the profiles of the parameters on the cross-section of the inlet are determined according to the overall design or by measurement. The boundary conditions on the cross-section of the outlet are not needed.

The transport coefficients change significantly near the solid wall. Large amounts of nodes should be carefully arranged near the wall for more precise calculations of the parameters which increase significantly the amount and the time of numerical calculations. We have used the surface function [4] to determine the boundary conditions at the wall. With the assumption of axial-symmetry, the radial velocity on the central axis is zero and the radial derivations of other parameters are zero.

IV. RESULTS OF CALCULATIONS

1. The effects of the parameters at the inlet on the results of calculation.

During design stage, the total flow rate at the inlet of the afterburner diffuser, bypass ratio and the temperatures of other parameters of the inner and outer flows can be obtained according to the overall design. However, since the velocity profile of the flow and the magnitude of the turbulence energy at the inlet are not available, we have first studied the effects of the velocity

profiles and the turbulence energy at the inlet on the calculation of the flow field.

(1) The effect of inlet profiles of axial velocity components on the flow field calculation

Figure 2 shows the effect of inlet profiles of axial velocity components on velocity fields under the condition of a constant flow rate, bypass ratio and inlet turbulence energy. The figure shows the calculated velocity profiles on cross-sections CM and CM' based on three inlet profiles of axial velocity. The dash line is the result with the assumption that the velocity profiles of the inner and the outer flows are hyperbolic and there is no backflow at the downstream side of the center cone. The dash and dot line is the results having uniform distribution of the velocity at the inlet and a small backflow region at the downstream side of the center cone. Obviously, the results of both extreme cases deviate greatly from the measured data. The solid lines in the figure show the calculated results using the measured velocity profile near the inlet cross-section (cross-section Z shown in Figure 1) as the velocity at the inlet. The calculated results are very close to the measured data except those in the region at downstream sides of the annular confluent ring.

The measured velocity profile at cross-section Z (the figure is not shown here) shows that the axial velocity profiles of the inner and the outer flows are very close to uniform distribution. However, the velocity of the inner passage flow in the region near the center cone is significantly lower due to the effect of the turbo wheel located upstream and the possible lower velocity at the base of the blades. Therefore, the assumption with a uniform or a hyperbolic velocity profile at the inlet cannot provide satisfactory results.

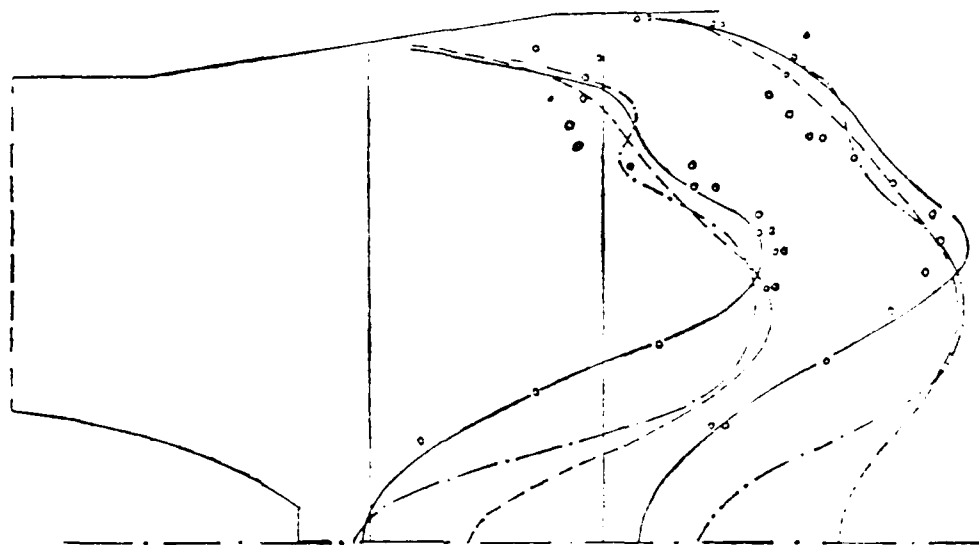


Figure 2. Effect of inlet profiles of axial velocity component on the velocity field

The cause of deviation of the calculated results from the experimental results in the downstream region of the annular confluent ring is discussed in the following. The velocities were measured using a pitot tube in the experiments. There are many limits in using the pitot tube to measure the velocity, such as that the angle between the velocity and the pressure opening should not be too big, the turbulence intensity should not be too high, etc. Calculations have shown that the angle between the direction of the velocity and the pressure opening is over 7° and the turbulence intensity is over 30% in some regions at the downstream side of the annular confluent ring. Beer, et al. [5] indicates that the error of the measured velocity by the pitot tube is significantly large when the turbulence intensity is larger than 20%. Presently, there is no reliable method to make the correction. Although the distribution of the grids is not dense enough at the downstream side of the annular confluent ring, the calculated trend is reliable.

The effect of inlet profiles of axial velocity on the temperature field is very small.

(2) The effect of inlet turbulent energy on the calculated results.

Figure 3 shows the effect of the inlet turbulent energy on the velocity field. Four velocity profiles calculated from four different turbulent energies are shown in the figure. The values of the four turbulent energies are

- | | |
|-------|--|
| No. 1 | $k_1 = 0.005\bar{u}^2$, $k_2 = 0.005\bar{u}^2$; |
| No. 2 | $k_1 = 0.005\bar{u}^2$, $k_2 = 0.0005\bar{u}^2$; |
| No. 3 | $k_1 = 0.005\bar{u}^2$, $k_2 = 0.15\bar{u}^2$; |
| No. 4 | $k_1 = 0.008\bar{u}^2$, $k_2 = 0.15\bar{u}^2$; |

where k_1 and k_2 are the turbulent energies of the flows in the inner passage and the outer passage, \bar{u} is the average velocity at the inlet of the diffuser. Keeping the turbulent energy of the inner flow at $0.005\bar{u}^2$, the change of the turbulent energy of the outer flow has significant effect on the velocity profiles at the downstream side after the center cone and the annular confluent ring. Reducing the turbulent energy of flow in the outer passage, the backflow region after the conic frustum increases and extends significantly and the downstream velocity profiles after the annular confluent ring become non-uniform. This is because the extent of gas mixing decreases with decreasing turbulence energy. Similar effects are obtained with reducing the turbulent energy of the inner passage flow.

2. The calculated flow field in the diffuser at various rotating speeds on the ground.

After studying the effect of the inlet parameters on the flow field, we have found that the inlet parameters of the afterburner diffuser of certain models of turbofan can be obtained by using the experimental values for the axial velocity, letting the radial velocity equal zero, using average value for the temperature of the outer pass flow and 1.2% of the average energies of the inner and outer pass flows as the respective turbulent energies.

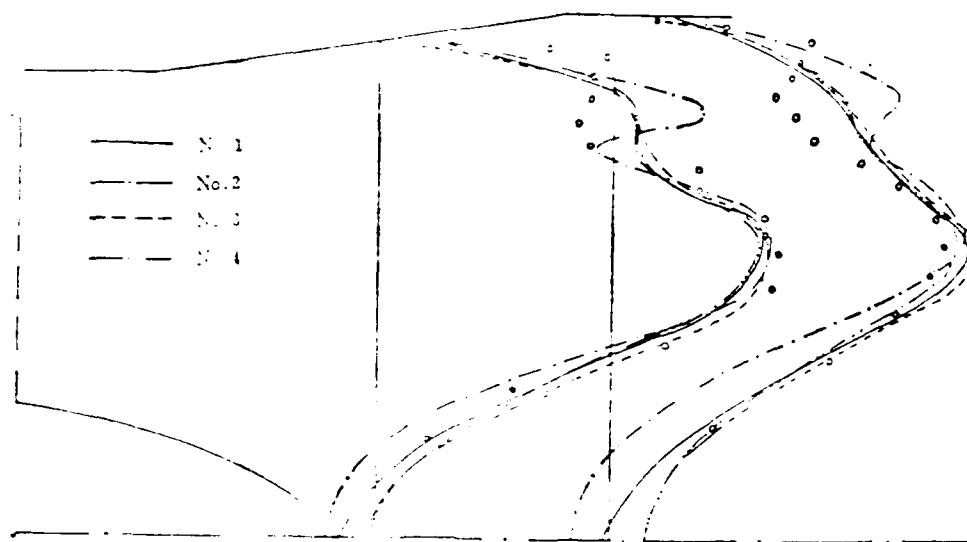


Figure 3. Effect of inlet turbulent energy on the velocity field.

The dissipation of the inlet turbulent energy is given by the following equation:

$$\epsilon = 0.001 \cdot \frac{U^3}{R} \cdot \rho \cdot g$$

where R is the radius of the afterburner.

Figure 4 shows the velocity field calculated based on the above inlet conditions and at rotating speeds of 0.97, 0.93 and 0.87. The corresponding experimental data are shown in the figure for comparison. It shows that the calculated results are consistent with the experimental results. However, some deviation occurs at a low rotating speed since the turbulent energy is small. The calculated flow field is correct when proper inlet parameters /59 are given.

The flow fields at various rotating speeds show that the velocity profiles of the diffuser at different speeds are similar. However, the value of the velocity increases and the profile becomes sharper with increasing rotating speeds because the flow rate increases and the bypass ratio decreases with increasing rotating speed.

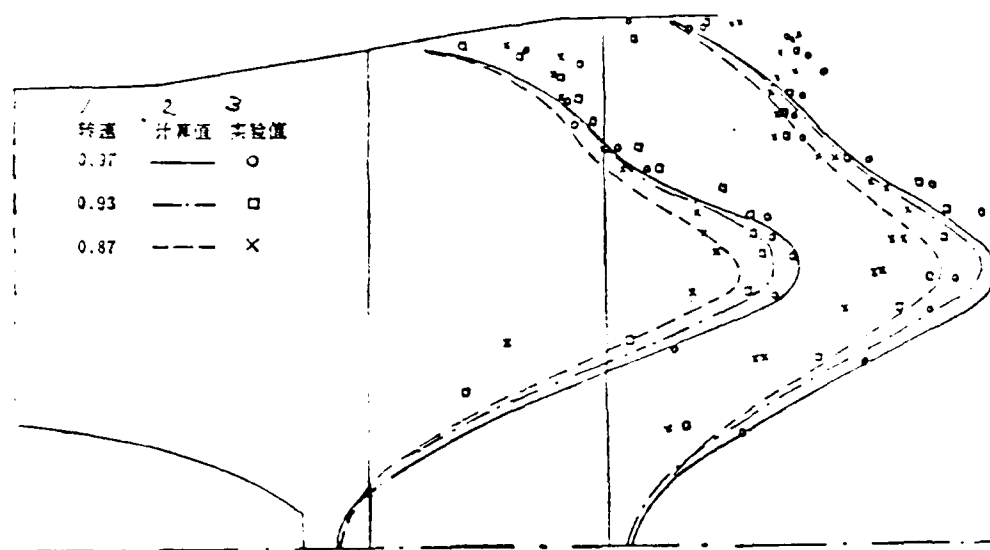


Figure 4. Velocity field at various rotating speeds of the engine.
1--rotating speed; 2--calculated value; 3--experimental data

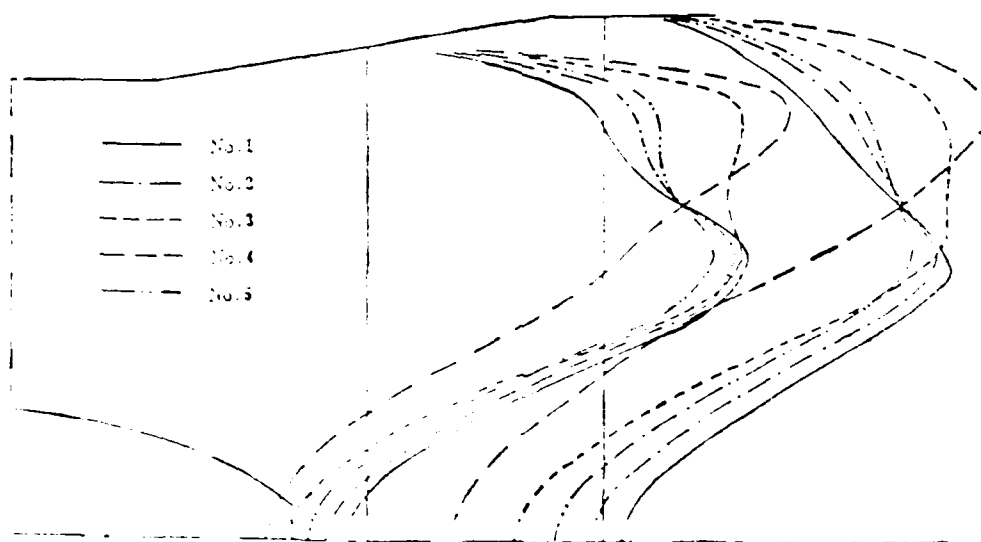


Figure 5. Velocity field in various states of flight.

3. The flow field calculated at various states of flight.

The experimental data of the inlet profile of axial velocity component of the diffuser under flight conditions are not available. The ground tests at various speeds have shown that the

velocity profiles are similar at different rotating speeds and values of velocity. It can be assumed that the inlet profiles of axial velocity of the diffuser are also similar during flight. The value of the inlet velocity profile depends on the flow rate and density. Other parameters can be determined similar to those discussed in the previous paragraph.

Figure 5 shows the calculated velocity fields at five different states of flight. The parameters corresponding to the five states of flight are listed in Table 2. The figure shows that the velocity field depends mainly on the bypass ratio at various states of flight. At altitude of 15 km, $M = 2.6$ and bypass ratio of 1.9578, the outlet velocity profiles are not uniform and the air flow in the outer pass has a peak. The velocity decreases rapidly with the decrease of radius. Near the inlet of the diffuser, the flow separates at the surface of the center cone and a large region of backflow is formed. The velocity field is more uniform at the altitude of 19 km, $M = 2.0$ and bypass ratio of 1.4368. A maximum in the velocity profile of the inner flow appears when the bypass ratio decreases continuously. Decreasing the bypass ratio, the velocity in the inner pass increases while the velocity in the outer pass decreases and the region of backflow behind the center cone diminishes gradually.

TABLE 2. Inlet parameters in various states of flight.

1 No.	2 State	3 Altitude (km)	4 Mach Number	5 Flow ratio to the ground test	6 T ₁ (K)	7 T ₂ (K)	8 p ₀₁ (Pa)
No. 1	0	0	1	1.000	288	375	1.934×10^5
No. 2	0	0.89	1.342	1.075	286	457	2.678×10^5
No. 3	15	0.6	0.935	1.9578	220	550	1.743×10^5
No. 4	19	1.0	0.930	1.4368	220	454	0.539×10^5
No. 5	22	1.4	0.933	1.242	225	421	0.262×10^5

1--parameters; 2--states; 3--flight altitude; 4--flight Mach number; 5--flow ratio to the ground test; 6--bypass ratio

V. CONCLUSIONS

1. The calculated results are consistent with the experimental data except in the downstream region after the annular confluent ring. The results indicate that our mathematical model is correct. A new method of measurement of the flow field should be used to further test the accuracy of our calculations.

2. Calculation shows that the flow field in the diffuser is affected significantly by the profiles of the inlet parameters. Therefore, a precise modeling of the inlet flow field is very important to perform experiments on models or parts.

3. Numerical calculations accompanied with experimental results can be used to study the flow field of the diffuser with significant savings on manpower, material cost and the time of research.

REFERENCES

- [1] Patankar, S. V., Spalding, D. B. A calculation for heat, mass and momentum transfer in three-dimensional parabolic flow, *Int. J. Heat, Mass Transfer*, Vol. 15, P. 7887, (1972).
- [2] Chen, Y. L., Sun, Ci. "The Convergency of the SIMPLE Method". *Journal of Engineering Thermal Physics*, Vol. 5., No. 3 (1984).
- [3] Launder, B. E., Spalding, D. B. *Mathematical Model of Turbulence*, Academic Press, London and New York (1972).
- [4] Patankar, S. V., Spalding, D. B. *Heat and Mass Transfer in Boundary Layers*, Int. Textbook Company Ltd., London (1970).
- [5] Beer, J. M., Chigier, N. A. *Combustion Aerodynamics*, Applied Science Publishers Ltd., London, (1972).

Design of an Airborne Optic Fiber Data Bus System

157

Fan Renzhou, Wang Gonghao, Chen Ruilin

(Beijing Institute of Aeronautics and Astronautics)

Abstract

The development, application, communication protocol and system structure of an airborne data bus system are discussed in this paper with emphasis on the design of hardware, software and optical fiber transmission system of the bus controller and remote terminal. Some experiments and their results are also given in this paper.

Introduction

Airborne, time-sharing multiplex transmission data bus was first used in the early 1970's on such piloted aircraft as B-1[1], A-7[2] and F-15[3] as well as on spacecraft[4]. A digital information system composed of the standard bus is widely used on the spacecraft, aircraft, warships and tanks. With the computer as the centerpiece, the optic fiber transmission as its medium, the distributed digital avionic information system that is redundant, fault-tolerant has become the hallmark of a new generation of avionic system structures. The airborne data bus is one of the central components, which has the following fields of application:

1. To be used in the digital avionic information system, DAIS^[5,6], in which a double redundancy data bus is used, providing information transmission, control and display to meet the requirements of various types of aircraft and flying missions.

2. To be used in an aggressive-controlled technique CCV in a statistically controlled placement, in which the CCV uses a data bus having triple redundancy (or quadruple redundancy) to implement digital teletype/optical transmission controls. On spacecraft, a data bus having quadruple redundancy is used to improve reliability of long duration flights.

3. To be used in a distributed computer composed of microcomputers.

4. To be used as a component in the monitoring system providing integrated telemetry remote control data and graphic transmission.

5. To be used in the ground integrated hot bench^[9,10] in an aeronautical, and astronautical electronic system.

II. System Structure and Communication Protocol

1. System Structure

Figure 1 shows the block diagram of the airborne data bus. It comprises the bus controller, bus monitor unit, remote terminal and the transmission network. The bus controller controls and supervises the entire work of the bus, while the bus monitor unit monitors whether there is any fault in the

information transmission through the bus. The remote terminal receives and responds to the commands and implements network communication. The transmission medium is either an electrical transmission line or an optical fiber with a coding rate of 1 Mb/s.

2. Control Mode of Information System

This means how information is being dispatched and transmitted in the network. There are several modes which include the time-sharing mode[11,12], the instruction responding mode and the ballot-casting competition mode.

158

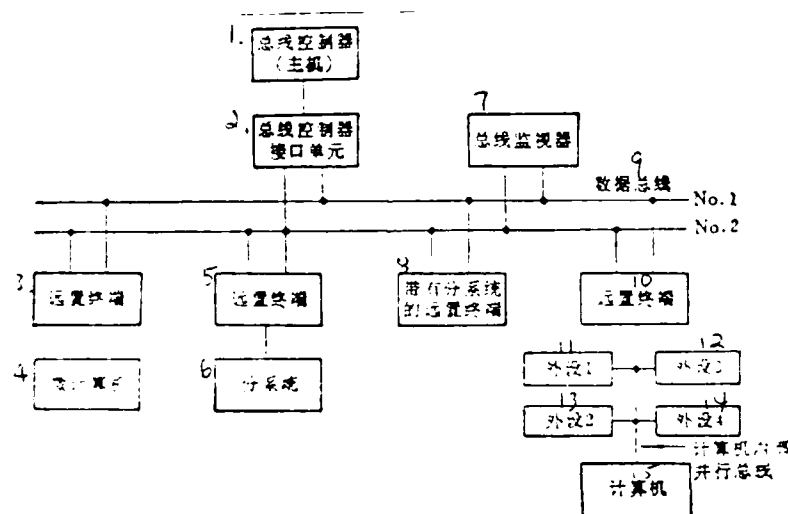


Figure 1. The Block Diagram of Airborne Data Bus

1. bus controller (host computer)
2. bus controller (interface unit)
3. remote terminal

4. microcomputer
5. remote terminal
6. subsystem
7. bus monitor
8. remote terminal with subsystem
9. data bus
10. remote terminal
11. peripheral equipment 1
12. peripheral equipment 3
13. peripheral equipment 2
14. peripheral equipment 4
15. computer
16. computer built-in parallel bus

The most commonly used mode today is the instruction-responding mode, in which there is only one master dispatch terminal in the network. The rest are remote terminals. Instruction is transmitted by the master dispatch terminal and is responded to by other terminals to implement network communications, system testing and real time duplication.

3. Forms of Network

The form of network affects the quality of communication, response time, expandability, resistance against destruction, etc. The form can be annular, star-shaped (radial), K-shaped and others. The annular loop when broken becomes straight-line shaped. The annular and linear forms are usually used for electrical transmission lines while the star-shaped (radial) form is more commonly used in optical fiber network.

4. Types of Code and Synchronization

Types of codes suitable for use with optical fiber channel include Frequency Shift Code (FSC). Frequency Shift Keying Code; Modified Frequency Shift Keying Code (MFSK); Phase Shift Keying Code (PSK); Modified Phase Shift Keying Code (MPSK) and etc.[13]. The code type for the bus is PSK, which is also known as Manchester Code whose characteristic is that its line-transmitted coding signal direct current component is equal to zero (when modulated by bipolar level and used in cable transmission) or the direct current level is of constant value (when modulated by unipolar level and used in optical fiber transmission). Also included in the information stream of this coding is the information of bit synchronization.

Word synchronization: For short distance, multi-user network communication, word synchronization should be as simple as possible, pseudo-random code is not used in this case. Instead, a positive pulse of $1.5\mu\text{S}$ and negative pulse of $1.5\mu\text{S}$ are used to form the word synchronization code, which can play an advance guiding role that can lead to the solution of the problem of initial phase ambiguity in the absolute phase modulation. The problem of data transmission in the asynchronized network can be better resolved with the aid of this synchronized code.

5. Communication Protocol[15,16]

The U.S. Military Specification MIL-STD-1553B for bus standard prescribes communication protocol as follows: The bus is of the command-responder type. There should be independent

at the various terminals, the network operates on asynchronous working mode, command is given by the bus controller and is responded to by the terminal at the selected site. A time-sharing multiterminal half-duplex communication is thus achieved. Information is transmitted through the bus as units of "message". By message is meant each command transmitted by the controller. The terminal responds to the command, completing the transmission of one group of data and a set of status words. A message is comprised of a certain number of words. There are three types of words: instruction word (dispatch signal), status word (shake-hand signal) and data word. Figure 2 shows the structure of the words.

There are three types of message formats: the data transmission type, mode control type and the broadcast transmission type.

(1) Data Transmission Type: With this type of transmission, it is possible to implement communication between the controller and the terminal and vice-versa, also between the terminals. The message format is shown in Figure 3.

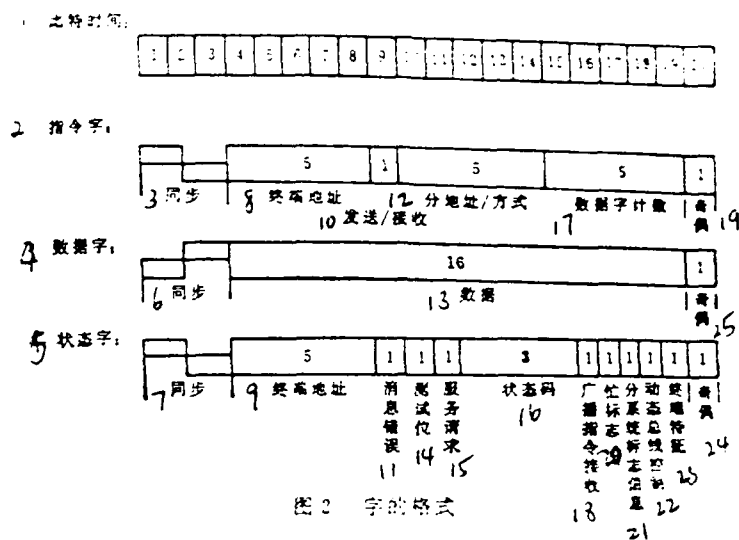


Figure 2. Word Format

1. bps (bits per second)
2. instruction word
3. synchronization
4. data word
5. status word
6. synchronization
7. synchronization
8. terminal address
9. terminal address
10. transmitting/receiving
11. message error
12. sub-address/mode
13. data
14. test point
15. service request
16. status code
17. data word count
18. broadcast instruction receiving
19. parity
20. busy mark
21. subsystem marking information
22. dynamic bus control
23. terminal characteristics
24. parity
25. parity

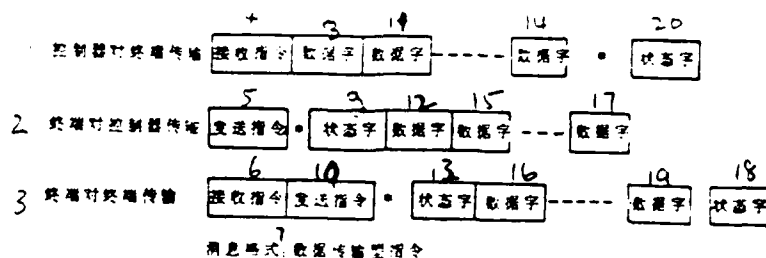


图3 消息格式 (注: *表示响应时间4~12μs)

Figure 3. Message Format
(Note: * indicates response time 4-12μs)

1. controller to terminal transmission
2. terminal to controller transmission
3. terminal to terminal transmission
4. receiving instruction
5. transmitting instruction
6. receiving instruction
7. message format: data-transmitting instruction
8. data word
9. status word
10. transmitting instruction
11. data word
12. data word
13. status word
14. data word
15. data word
16. data word
17. data word
18. status word
19. data word
20. status word

(2) Mode Control Type: In this type, the mode command is given by the bus controller. The working mode can be changed to achieve dynamic control of the bus, bus redundancy control, the repetitive construction of the system real time and self-testing of terminals etc.

(3) Broadcast Transmission Type: Broadcasting command is given by the bus. All terminals capable of receiving the broadcast command can simultaneously receive the broadcasting command and data, thus making message transmission faster and more effective.

Foremost requirements of the protocol are that terminals must respond to the status words within 4-12 μ s and that they have to implement numerous modes of commands.

III. Design of System Hardware

The system hardware is comprised of the following: the bus control main processor MP, bus controller interface element BCIU, the remote terminal RT, the subsystem interface SSI, the optical fiber communication system, etc. Our design philosophy is to make possible that the BCIU and RT could be interchangeably used, having intelligence, energy and interfaces for numerous 16-digit microcomputers (8086, 9900, Z8000) or 8-digit microcomputer (8085, Z80).

1. MP, BCIU and RT

There is a dual-channel communication pool interface between the MP and the BCIU. MP transmits the bus control block to the communication pool; informs the BCIU to fetch the information, interprets it and executes accordingly; completes the bus communication process and sends back to the MP the status words and data via the communication pool, achieving the aggressive working mode, improving bus communication efficiency.

Figure 4 shows an intelligent terminal formed by 8086 or

9900, the upper half is the RT while the lower is the SSI. There is a microprogram controller in the RT which performs sequential control over the transmission/receiving of the terminal, senses and distinguishes the various modes of message transmission on the basis of which to determine the different working sequences of the terminal. The microprogram controller can also produce self-checking sequence; implement self-testing of the terminal. The intelligent terminal that includes a microprogram controller will perform both as the RT and the BCIU. It can also carry out a self-testing operation.

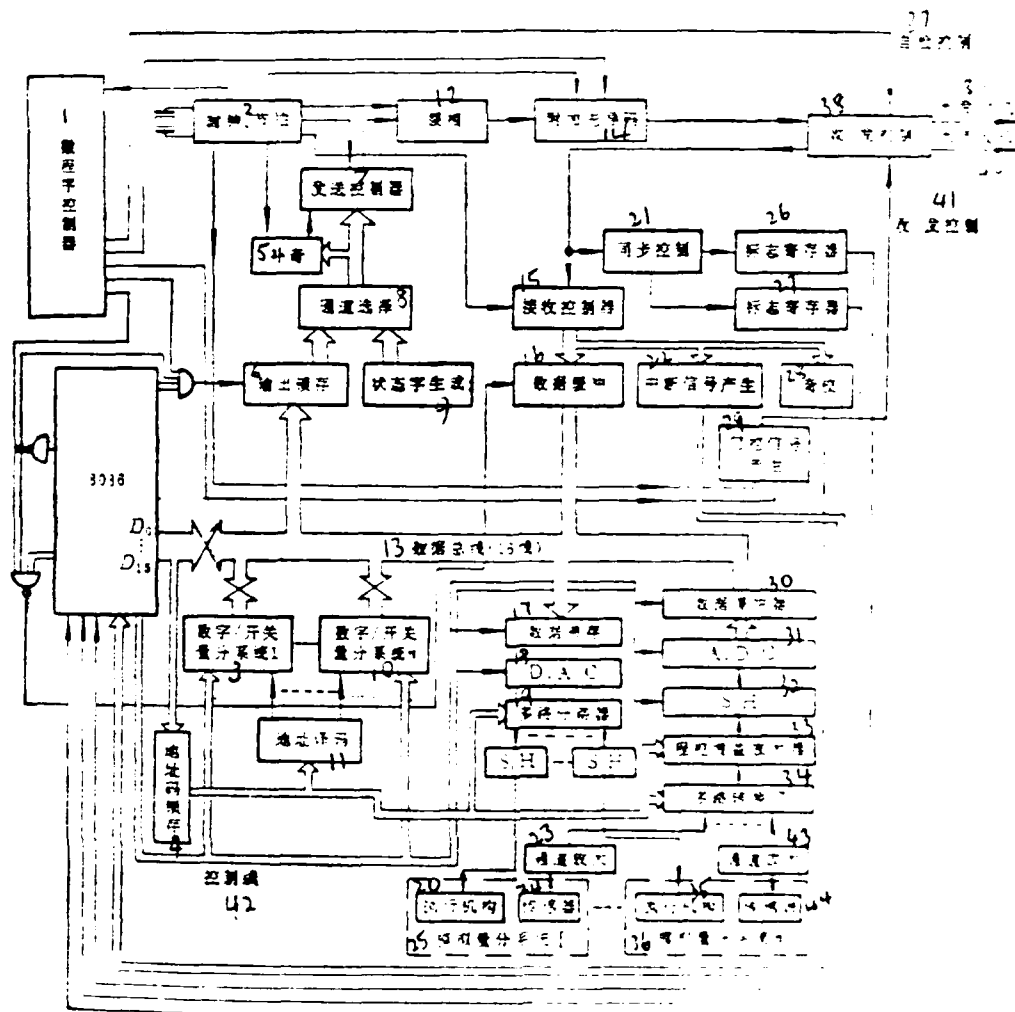


Figure 4. RT Block Diagram

1. microprogrammed control unit
2. clock, beat
3. digit/switch sharing system 1
4. address code storage and feed
5. odd-complement
6. output feed and storage
7. transmitting controller
8. channel selection
9. status word formation
10. digit/switch sharing system
11. address decoding
12. phase splitting

13. data bus (16 lines)
14. extra advanced code
15. receiving controller
16. data buffer
17. data storage
18. D.A.C.
19. demultiplexer
20. executing mechanism
21. synchronization control
22. producing interrupt signal
23. channel amplification
24. sensor
25. analog assignment subsystem
26. mark register
27. mark register
28. odd-check
29. producing gate controller signal
30. data buffer
31. A.D.C.
32. S/H
33. program-controlled gain amplifier
34. multiplexer
35. executing mechanism
36. analog assignment subsystem
37. self-checking control
38. receiving/transmitting control
39. optical (light) emitter
40. optical (light) emitter
41. receiving/transmitting control
42. control line
43. channel amplification
44. sensor-transducer

2. Optical Fiber Communication System

The optical fiber communication is provided with a high code rate that can reach as high as 1-1000 Mb/s, excellent transmission quality with bit error rate less than 10^{-9} - 10^{-12} , immunity against electromagnetic disturbance and nuclear radiation and other features. It is the most promising means for airborne data and picture transmission. The airborne optical fiber communication network is a close-distance, multiport network. Light emitting diode (LED) is chosen as the optical transmitter and PIN as the optical receiver. An eight-port

transmission-type double-cone coupler is used. The distance of action between terminals is 200 meters, the bit error rate is less than 10^{-9} . The key problems with the optical fiber network are: a need to increase the number of ports of the Star coupler, to reduce insertion loss and the non-uniformity of distribution of the optical power to solve the problem of the gradual drifting of the bus coding optical signal as responded to by the optical receiver, and to reduce bit errors in the decoding operation by using the instantaneous step-change type automatic gain control, etc. /61

IV. Design of System Software

The software structure of the system is a three-level functional distributed system; the main processor (MP) and the bus control processor (BCP) are all of the vertically distributed structure. The structural relationships between the BCP and various terminals (RTCP) are horizontally distributed. The monitor processor (MCP) is the exclusive fault-tolerant processor for monitoring the system.

From the top to the bottom, the system is working on the master-slave synchronization mode. While from bottom up to the top, the system works on asynchronous on-demand mode. The main processor operates on the time-sharing and phase-sharing system, incorporating bus control phase and main processor phase. The communication control process is executed in the bus control phase, while the process of the various sequences of operation of the bus control phase is executed in the main processor phase.

The bus control block (BCB) transmitted from the main processor is interpreted and executed by the bus controller. The implementation of communication, state monitoring, retrying of errors, supervision of redundancy etc., are carried out in conformity with the MIL-STD-1553B specification. Synchronization is achieved between MP and BCP. In addition to implementing the conventional task of various nodes, RTCP receives commands from the bus by the interrupt mode. It also transmits synchronous and asynchronous information as well as control of mode commands by the same mode.

number of BCB linked lists, etc. At the beginning of each minor cycle, MC, MP transmits a batch of BCB subsets to the communication pool, COMPL. The BCB subsets are concatenated according to the sequence required by the communication operations. The BCB block is processed when starting BCP on the interrupt mode by BCP. After BCB is processed in the minor cycle, BCP returns to its background bus supervisor.

1. System Software of MP

(1) Figure 5 shows the data structure of MP system in which

BCBB is the Bus Control Block Buffer zone

TAT the Terminal Addressing frequency Table

NAT subsystem Addressing frequency Table

BCBC Bus Control Block Chain

BCBC' auxiliary Bus Control Block Chain

MCR Minor Cycle Register

MCC Minor Cycle Counter

SPT System Parameter Table

EVT Event Table

(2) Programming Module: Table 1 shows level structure of software system operation

Table 1 Level (Layer) Structure of MP Software

LAYER		FUNCTION	MODULE
0 layer	1st level	surface block forming	PTBG, PTG, PNG, PBF, PWCG
	2nd level	BCB dispatch	QTS, QCG, QWP, QRP, QSC
1st layer		MP Time-sharing Phase-sharing	RBS, RMP, RPS
2nd layer		Command Execution	STAT, START, STEP, STOP, ATTACH, DETACH, DISPLAY SET
3rd layer		Language Interface	
Application Program			

0 layer; 1st level: the module forming the system's basic data structure is called the surface block forming layer such as TAT, NAT, table-filling modules, etc.

0 layer; 2nd level: the dispatching level of BCB, such as TAT scanning module, BCBC forming module, read/write COMPL module, etc.

Layer 1 (first layer) software: MP time-sharing, phase-sharing control process, such as bus dispatching module, MP traffic control module, etc.

Layer 2 software: MP command implementing module layer. When the system enters into the MP phase command processing segment, the command display system parameters can be used, the bus dispatch process executed once and a certain terminal connected or disconnected, etc.

Layer 3 software: Interface layer of a still higher level language capable of providing the application program with descriptive language and interpreter.

AD-A168 450

ACTA AERONAUTICA ET ASTRONAUTICA SINICA (SELECTED
ARTICLES)(U) FOREIGN TECHNOLOGY DIV WRIGHT-PATTERSON
AFB OH M LIU ET AL 29 MAY 86 FTD-ID(RS)T-1275-85

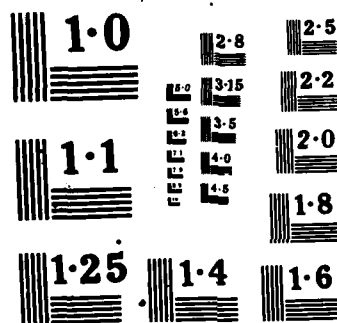
2/2

UNCLASSIFIED

F/G 20/4

NL





NATIONAL BUREAU OF STANDARDS
MICROCOPY RESOLUTION TEST

2. BCP, RTCP Software

There are foreground and background jobs in BCP operations. The foreground job interprets, executes BCB subsets within the COMPL. The background job supervises, monitors the bus. BCP starts processing BCB during each minor cycle. It also transmits /63 bus instructions; transmits and receives data; predicates RTCP status words; decides retrying provisions; and finally produces status words. Background job resumes when all BCB block processing has been completed during the minor cycle.

RTCP acquires, controls and monitors data of the subsystems controlled by RTCP, executing their respective processing programs NHR. The processing programs of the subsystems are all done through their respective control blocks and the common data communication band, DCB, implementing control over the controlled devices. RTCP produces interrupt signals soon after it receives bus command from BCP and rolls in bus service program BCR to implement bus communication. RTCP returns to acquisition and monitor program when the tasks are completed.

V. Conclusions

On-line testing of the system shows that the entire system is capable of implementing the airborne data bus communication protocol to accomplish the task of data communication. Except for the microcomputer which is introduced from abroad, all other components used in this system, including optical fiber communication network are locally developed. Experimental use has shown the design is rational and correct. Further research

on system structure, communication, large scale integrated hardwares, system software as well as reliability of the system, etc., are left to be done in the future with a view to implementing engineering application at an early date.

Acknowledgement is made to Messrs Wu Jiaxin, Cao Deshu, Yu Zirong and Wang Dong of the Institute of Laser Communication Research for their endeavors in the development network system that comprises 8086.

References

- [1] B-1 Avionics Data Multiplex System, AD A033793, p. 15.
- [2] The Application of Multiplexing to the A-7D Aircraft, AD 915600.
- [3] The Design and Development of the F-15 Avionics Data Bus, AD A033793, pp. 3-15.
- [4] Space Shuttle Multiplex Data Bus System, AD A033793.
- [5] Integrated System Design-DAIS, WESCON, 1978, 11.4, pp/ 1-16.
- [6] Digital Avionic Information System (DAIS) Multiplex System, AD A033793, pp. 99-118.
- [7] Multiplex Data Buses as Applied to the DAIS Flight Control System, AD A033793, pp. 119-132.
- [8] Fiber Optics Application in the Shipboard Data Multiplex System, AD A039505.
- [9] The Development and Evolution of a Multiplex Data Bus System for Advanced RPV Applicationd, AD A033793, pp. 255-265.
- [10] A Modular Spacecraft Communications and Data Handling System, AD A033793, pp. 237-254.

- [11] An Optical-Fibre Multi-Terminal Data System for Aircraft,
AD A068310, p. 763.
- [12] Shipboard Data Multiplex System Advanced Development Model,
Contract No. 024-74-C1200.
- [13] The Code Suited for Data Transmitting at High Speed in
Optical Fiber, Electronic Design, October 25, (1978),
Vol. 26, No. 22.
- [14] Fan Renzhou: A computer-controlled programmable YK-1
as Monitor System for General Industrial Use. Technical
Summary HB-F191, Beijing Institute of Aeronautics and
Astronautics.
- [15] MIL-STD-1553A, AD A033793, p. 469.
- [16] MIL-STD-1553B, AD A068310, p. 823.
- [17] MIL-STD-1553 Fiber Data, AD A033793, pp. 177-235.

END

Dtic

7-86